Contamination Induced Continuous-Wave Laser Damage of Optical Elements

A THESIS
SUBMITTED TO THE FACULTY OF THE GRADUATE SCHOOL
OF THE UNIVERSITY OF MINNESOTA
BY

Andrew Kyle Brown

IN PARTIAL FULFILLMENT OF THE REQUIREMENTS
FOR THE DEGREE OF
DOCTOR OF PHILOSOPHY

Joseph Talghader

June, 2018

Acknowledgements

There are many people and organizations that have contribution to this research and my time in graduate school. I would like to thank my advisor Dr. Joseph Talghader for guiding me throughout graduate school. Your patience, expertise, and advice have been invaluable and I am indebted to you.

My colleagues Kyle Olson, Lucas Taylor, and Tirtha Mitra contributed significantly to this research and their efforts as well as friendships are greatly appreciated.

Dr. Albert Ogloza was instrumental in this project from start to finish. Your contribution to my research and time in graduate school cannot be overstated.

Jeff Thomas, Dave Bernot, Lucas Forster, and Joseph Randi at Penn State's Electro Optic Center provided key experimental support for laser damage testing. Without their help this research would not have been possible.

My fellow students: Phil Armstrong, Jordan Burch, Wing Chan, Avijit Das, Anand Gawarikar, Sangho Kim, Mint Kunkel, Jon Lake, Yu-Jen Lee, Phyo Lin, Merlin Mah, Caitlin Race, Sara Rothwell, Ryan Shea, Joe Stansbery, and Brad Tiffany. You were vital for your ideas, support, and my entertainment.

Funding for this research came from the Joint Technology Office (JTO) under Office of Naval Research Grant N00014-12-1-1030. In addition, The Directed Energy Professional Society provided much appreciated financial support to me as well as a friendly form at which I presented much of my research.

The University of Minnesota's Nano Center and Characterization Facility were heavily used for for sample preparation and characterization. Special thanks to Bashir Jama, Nicholas Seaton, and Paul Kamani.

And finally to my parents. You have always nurtured my curiosity and supported me without judgment. Words are inadequate to describe my thanks.

Dedication

To my friends from Michigan Tech and elsewhere.

Abstract

Continuous-Wave laser-induced optical breakdown affects anyone whose work requires tightly focused light, high power sources, or delicate materials. It often occurs unexpectedly and seemingly randomly at optical intensities far lower than those predicted by ultra-short pulse laser experiments. Further complicating the issue is that the majority of laser damage experiments use carefully controlled laboratory conditions with short-pulsed lasers focused to small spots on clean, pristine materials. Continuous-Wave laser damage is usually attributed to contamination, and occurs under radically different conditions. To determine the origin of contamination-induced breakdown, microparticle contaminated optics were stressed using a 17 kW continuous-wave laser. Contamination-induced breakdown occurred at intensity levels many orders of magnitude lower than expected in clean, pristine materials. For both half-wave and high reflectivity coatings, damage thresholds were found to strongly follow the bandgap energy of the film. It is theorized that surface contamination heated by the laser thermally generates free carriers in the films. If the free carrier concentration exceeds a certain threshold, runaway absorption and breakdown will occur. A thermal model incorporating the particle absorption, interfacial heat transfer, and free carrier absorption was developed, and it explains the observed data. The bandgap of the film, the absorption and thermal contact of the contaminant, and the evaporation time of the particle, all determine whether a material can survive. The observed bandgap dependence is in direct contrast to the behavior observed for clean samples under continuous wave and long-pulse illumination, and, unexpectedly, has similarities to ultra-short pulse breakdown for clean samples, albeit with a substantially different physical mechanism. These findings strongly suggest that low bandgap materials are a liability in optics exposed to environmental contamination. Laser conditioning was examined as a means of preventing damage by removing contamination without initiating damage. Absorption measurements taken using photo thermal common-path interferometry show up to a 90% absorption reduction with conditioned samples. Regular laser conditioning at low irradiances can prolong the life of optics that must operate in difficult environmental conditions.

Contents

Acknowledgements **i**

Dedication **ii**

Abstract **iii**

List of Tables **vi**

List of Figures **vii**

1 Introduction **1**

1.1 Motivation 1

1.2 Outline 2

2 Laser Damage History and Prior Research **4**

2.1 Introduction 4

2.2 Pulsed Laser Damage 5

2.3 Continuous-Wave Laser Damage 11

3 Laser Damage Testing: Initial Experiments **16**

3.1 Experimental Set-Up 16

3.2 Samples Tested 19

3.3 Test Results 22

3.4 Particle Studies 27

4 Quantifying Laser Conditioning using PCI **33**
4.1 Introduction . . . 33
4.2 Photo Thermal-Common Path Interferometry . . . 34
4.3 Initial Conditioning Experiments . . . 39
4.4 Conditioning Measured in Real Time . . . 41
4.5 Refining Contamination and PCI Measurement . . . 43
4.6 Conditioning Results . . . 45
4.7 Discussion of Laser Conditioning . . . 48
4.8 Laser Conditioning Summary . . . 49
4.9 Free Carrier Absorption in Microheater Films . . . 50

5 Bandgap Dependence of CW Particle Induced Laser Damage **52**
5.1 Motivation and Prior Research . . . 52
5.2 Optics and Contaminants Tested . . . 53
5.3 LIDTs vs. Bandgap: Results . . . 56
5.4 UV Plank Emission: Free Carrier Generation . . . 57
5.5 Capping Layers . . . 60

6 Thermally Generated Free Carrier Breakdown Model **63**
6.1 Heat Transfer into the Optical Coatings . . . 63
6.2 Heat Equation with Free Carrier Absorption . . . 65
6.3 Material Properties in Model . . . 66
6.4 Solving the Heat Equation Numerically . . . 66
6.5 Discussion . . . 69
6.6 Conclusion . . . 72

References **73**

List of Tables

5.1 IBS coatings: material properties 54
5.2 IR + UV exposure results 60
6.1 Fitting model TCCs to experimental data 68

List of Figures

2.1 Pulsed laser breakdown mechanisms 6
2.2 Keldysh parameter: tunneling and multiphoton absorption 7
2.3 Pulsed damage: Thermal damage vs. fracture and ablation 9
2.4 LIDTs vs pulse length: $\tau^{1/2}$ dependence 9
2.5 Pulsed LIDTs vs. material bandgap energy 10
2.6 Actively cooled mirror design 12
2.7 E-beam, IBS, and ALD coating deposition processes 13
2.8 Particle plasma formation and thermal shock 15
3.1 Penn State Electro-Optics Center Lab 18
3.2 Damaged optic and melted mount 19
3.3 Hafnia-silica DBR and typical laser damage craters 20
3.4 Silica and gold contamination: sample heating 20
3.5 Typical surface carbon contamination density 21
3.6 Laser testing grid 22
3.7 Clean vs. dirty optic temperature 23
3.8 Laser exposed carbon particle flash spectrum 23
3.9 Drag wipe cleaning surface image 24
3.10 Drag wipe cleaning and sample heating 24
3.11 Sample temperature for first vs. second laser exposures 26
3.12 Sample temperature profile during exposure 27
3.13 Surface contamination before and after conditioning 28
3.14 Image processing for particle data 29
3.15 Particle size histogram before and after exposure 29
3.16 High speed images of particle evaporation 30

3.17 Conditioned residue surface topography 31
3.18 Surface image of conditioned residue 32
3.19 TOF-SIMS data of conditioned residue 32
4.1 Photo thermal common-path interferometer 34
4.2 PCI measurement basics 35
4.3 PCI beam paths 37
4.4 Conditioning measured within a laser spot 39
4.5 Conditioning during 2D repeat PCI scans 40
4.6 Increasing conditioning with higher irradiance line scans 40
4.7 Real time absorption change 42
4.8 SEM of 1 μm graphite flakes 44
4.9 Absorption reduction for 1 second exposures 45
4.10 Absorption reduction for varying exposure duration 46
4.11 Particle morphological changes with laser exposure 47
4.12 SEM of conditioned graphite particles 47
4.13 Microheaters used for free carrier absorption measurement 50
4.14 Measured free carrier absorption in silicon 51
5.1 PCI scan of carbon contaminated sample 55
5.2 High reflectivity DBR LIDTs vs. Bandgap energy 56
5.3 $\lambda/2$ coatings LIDTs vs Bandgap energy 57
5.4 $\lambda/2$ coatings after testing 58
5.5 UV + IR Laser damage experiment 59
5.6 Capping layers and backside sample illumination 61
5.7 LIDTs for tantala-silica DBRs with capping layers 62
6.1 Phonon bandgap reduction 67
6.2 Heat transfer and spherical symmetry approximation 67
6.3 Simulation using Matlab's PDEPE solver 68
6.4 Simulation meshgrid and boundary's 69
6.5 Simulation temperature profile and determining damage 70
6.6 LIDTs for $\lambda/2$ coatings compared to free carrier model 71

Chapter 1

Introduction

This thesis comprises the following work: Continuous-Wave (CW) laser damage testing of optical coatings with a variety of contaminants and a study of optical heating and particle change due to irradiation; Laser conditioning of optics using CW sources and absorption changes measured using photo thermal common-path interferometry; a newly observed bandgap dependence for particle-induced CW laser damage; and a thermal model incorporating free carrier absorption which describes particle induced laser damage. This work is preceded by a background chapter that briefly describes the mechanisms and differences between pulsed and CW laser damage, and why they must be treated independently.

1.1 Motivation

More advanced and efficient CW lasers are bringing a renewal of interest in directed energy systems. Critical to the performance of these systems are the optics required for beam shaping and steering. These optics must operate under large irradiances on the order of tens to hundreds of MWcm^{-2} and with very low absorption to prevent excessive heating, damage, and optical distortions from occurring due to the high operating power. While maintaining clean low absorption optics in controlled laboratory settings is feasible, high energy laser (HEL) systems are increasingly being called upon to perform in harsh environments where contamination is all but guaranteed. Unfortunately

environmental contamination often increases absorption to the point where particle induced laser damage creates a point of failure. When failure occurs, it is unpredictable with seemingly intact optics failing catastrophically without warning. In order for CW HEL systems to operate reliably in real world conditions particle induced laser damage must be understood and methods developed to negate its effects.

CW laser damage of optics has been a known problem and area of research for several decades. The development of high power chemical lasers in the 1970's and 1980's drove early research in the field. It was quickly recognized that the physical damage mechanisms of CW lasers were fundamentally different than that of pulsed lasers. Damage effects from ultra-short pulsed lasers are attributed to field-mediated effects whereas the longer operating time scales of CW lasers give rise to thermal effects. While there exists a body of literature for CW damage of pristine optics, there is comparatively little work done for non-ideal films with defects and less for contamination.

The goal of this research is to test contaminated optical coatings, simulating realistic operating conditions. The type of contaminant, the material properties of the coatings, and history of prior laser exposure, will all be considered in understanding their performance. It is hoped that this work will shed light on the fundamental physical mechanisms occurring on the surface of a contaminated coating and offer useful suggestions for future coating fabrication and laser operating procedures.

1.2 Outline

- Chapter 2 briefly presents the history and prior research of laser damage. The differences between pulsed and CW damage are highlighted and motivation as to why they must be treated independently is given.

- Chapter 3 examines laser conditioning of contaminated optics as a means of preventing damage. Photo thermal common-path interferometric measurements of absorption are used to quantitatively determine laser irradiances and durations required to effectively condition optics.

- Chapter 4 describes a newly observed bandgap dependence of particle induced CW laser damage. This dependence occurs for both half-wave and high reflectively

coatings and for two types of absorbing contaminants.

- Chapter 5 develops a model incorporating heat transfer and free carrier absorption to predict CW particle induced failure of optical coatings. This model closely matches the laser damage results from chapter 4.

Chapter 2

Laser Damage History and Prior Research

2.1 Introduction

Lasers have played a supporting role for many of the technological advancements of the past 60 years. Their unique high spectral and spatial coherence has allowed the research and the development of devices that would have been impossible to implement without them. In metrology, lasers have been used to measure everything from the distance to the moon, to 10^{-18} m contractions in the arms of the LIGO gravity wave detector. The extreme intensity which light can be focused has found uses in minimally invasive medical procedures, welding and cutting for industrial uses, and even controlled fusion. This intensity, combined with the speed and distance light propagates has been of military interest for decades. Lasers and fiber optics form the backbone of global communications. The bandwidth provided by modern fiber optic telecommunications cannot be understated.

While the high intensity produced by lasers has proved instrumental for many applications, this intensity must be handled by the optics controlling the emitted light, without materials breakdown. Any losses within the optics generate heat, changing the refractive index of the materials and degrading their optical properties. Worse still, if sufficiently high irradiances occur, optics can fail catastrophically, taking down the

entire laser system and leading to expensive repairs. Understanding the physical damage mechanisms that occur at the surface of an optic during damage is vital for the development of more reliable optics.

Laser damage can be broadly defined by two categories, pulsed and continuous-wave (CW). Pulsed lasers operate at low duty cycles, using a combination of Q-switching and/or mode locking. Q-switching prevents power from leaving the laser cavity while it is pumped, increasing the stored energy within the lasing media. Briefly allowing power to couple out of the cavity creates a short powerful pulse. Mode locking depends on different resonant modes within the cavity having a fixed phase relation to each other. For a brief moment, the modes constructively interfere to create an output pulse. Pulses generated by Q-switching and mode locking can be as fast as attoseconds, creating very high peak powers, irradiances, and electric fields. CW lasers provide a constant power output. Their peak power is much lower as the laser media gains and releases energy at a constant rate, however their average power is higher due to their 100% duty cycle. The vastly different timescales and peak powers of operation give rise to differing damage mechanisms. Pulsed and CW lasers must be treated independently for laser damage to be fully understood.

2.2 Pulsed Laser Damage

The vast majority of laser damage research has utilized pulsed lasers. One reason behind this is that pulsed lasers are capable of causing consistent damage in pristine optical coatings without any defects or contamination present. From a research perspective this is ideal as repeatable experiments can be conducted and a high degree of statistical certainty can be reported for a given coating. CW lasers currently do not have the power required to cause damage to many state-of-the-art coatings without a defect or absorption site present.

The exact mechanisms causing pulsed laser damage in dielectric materials are still up for debate. The most common mechanism presented as a means of initiating pulsed damage is multiphoton absorption [1, 2, 3, 4, 5]. For insulating metal oxides frequently used in optical coatings, their large bandgaps of 3-9 eV prevent any direct absorption of incident IR photons from the laser. If however large enough photon fluxes are present,

this can allow the statistically unlikely process where multiple photons being absorbed simultaneously and combine in energy. For optical films such as 4.3 eV bandgap tantalum pentoxide (tantala) and 5.7 eV bandgap hafnium oxide (hafnia), if four or five near-IR photons combine, their total energy is enough to exceed the bandgap, exciting an electron from the valence band into the conduction band of the material, see figure 2.1(a).

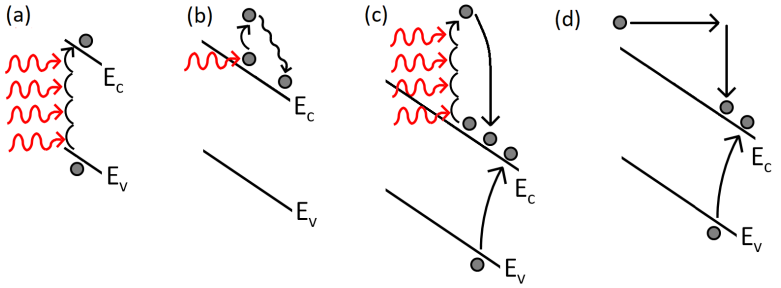

Figure 2.1: Physical processes occurring in a material under the large photon flux and high electric field of a pulsed laser. (a) multiphoton absorption of four photons combine in energy to excite a free carrier, (b) a free carrier absorbs a single photon, then thermally relaxes, releasing heat into the material, (c) a free carrier is excited by additional photons, then collides with the lattice, impact ionizing, creating a second free carrier, (d) a free carrier is accelerated by the electric field of the laser and impact ionizes, creating another free carrier.

Though the most widely reported, multiphoton absorption is not the only mechanism which can seed carriers into the conduction band. High electric fields cause the band edges to slant and shrink the effective distance that a carrier needs to tunnel through the bandgap [6, 4], see figure 2.2. Tunneling can work in tandem with multiphoton absorption to excite carriers, the ratio of the two described using the Keldysh parameter γ see equation 2.1, where ω is the laser frequency, e and m the electron charge and mass, c the speed of light, n the refractive index, E_g the bandgap, and ϵ_0 the free space dielectric permitivity. In the low frequency/photon energy limit, tunneling dominates as the the number of photons needed to combine simultaneously in order to exceed the bandgap is statistically unlikely. At higher frequencies/photon energy, fewer photons are needed for multiphoton absorption to excite free carriers above the bandgap, increasing the probability of multiphoton absorption.

$$\gamma = \frac{\omega}{e}\frac{mcn\epsilon_0 E_g}{I}^{1/2} \tag{2.1}$$

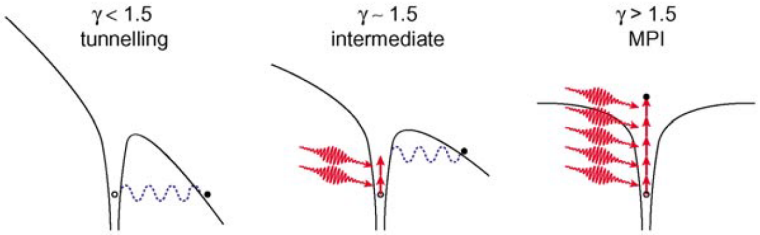

Figure 2.2: Tunneling and multiphoton absorption exciting carriers into the conduction band. Left: For small Keldysh parameters at low laser frequencies and strong electric fields, free carriers are generated through tunneling. Center: Intermediate Keldysh parameters see both tunneling and mulitphoton absorption contribute free carriers. Right: Large Keldysh paramters at shorter laser frequencies correspond with multiphoton absorption dominating carrier generation without requiring as high of electric fields. [4]

Free carriers by themselves will not cause any damage to the film, however their presence above the bandgap acts to seed events that can destroy the coating. The mechanisms occurring after multiphoton absorption depend on the electric field strength and thus the pulse length of the laser. For long laser pulses, over 10-20 ps, it has been found that energy per area required to damage (J/cm) increases as $\tau^{1/2}$, where τ is the exposure time. [7, 8, 1], see figure 2.4. This trend originates from heating caused from free carrier absorption and thermal transfer through the lattice. Once a free carrier has been created above the bandgap, it is free to absorb single photons from the laser as there is a continuum of states above the band edge that it can be excited to. The absorption of the material is now much higher. Free carriers gain energy, absorbing single photons, then release this energy as heat into the material, see figure 2.1(b). The shorter the pulse, the less time thermal conduction has to pull heat away from the laser spot, causing high temperatures and partial melting of the material, see figure 2.3(a).

Shorter pulses with larger photon fluxes begin to damage materials with additional, non-thermal effects. Free carriers already present from multiphoton absorption and/or tunneling are further excited by additional photons. If these carriers gain enough energy above the conduction band edge when they collide with the lattice and relax back down to the conduction band edge, the energy released is enough to excite an additional carrier

[2, 3, 5, 4], see figure 2.1(c). While multiple photons are required to gain this much energy, the continuum of states above the band edge allows this process to occur with discrete single photon absorptions rather the very improbable simultaneous multiphoton absorption. This process known as impact ionization or avalanching, creates many more free carriers, greatly increasing absorption and causes rapid heating of the material. Impact ionization can also occur from the high electric field present in the material. The electric field causes free carriers to be accelerated, gaining kinetic energy. When these carriers collide with the lattice, the released energy can excite a second carrier into the conduction band, see figure 2.1(d). The energy is deposited into the material from impact ionization occurs so quickly that it is essentially "frozen" in and does not have time to conduct away. This built up energy eventually couples to the lattice causing damage even after the initial pulse has passed [1]. The damage morphology caused by shorter pulses differs from the melting seen with longer pulses. Fracture and material ablation is seen in samples, see figure 2.3(b), and the laser induced damage thresholds (LIDT)'s begin to deviate from $\tau^{1/2}$, as the thermal transport becomes too slow to influence the rapid damage process.

Multiphoton absorption and impact ionization are both highly bandgap dependent. Impact ionization requires that a carrier gain energy greater than the bandgap in the short span between collisions with the lattice, while multiphoton absorption in a larger bandgap material requires additional photons to absorb simultaneously, increasing the photon flux required to make this statistically probable. Damage thresholds under pulsed irradiation follow a trend of increasing with larger material bandgap [3], see figure 2.5.

Another effect decreasing the overall damage thresholds of materials is self focusing. Absorption within the material creates localized heating and a positive change in the refractive index. This index change is undesirable as it can shift the wavelength at which coatings are most efficient and can cause problems for beam control. In thin films this is often not enough to cause create damage. For a thicker material however, the refractive index change acts as a thermal lens, focusing the laser energy to a tighter spot deep within the material, increasing the irradiance and the likelihood of damage. Thermal lensing also has positive feedback. Once an area has been heated and a thermal lens formed, the new tighter focus will further increase temperatures, the index change, and

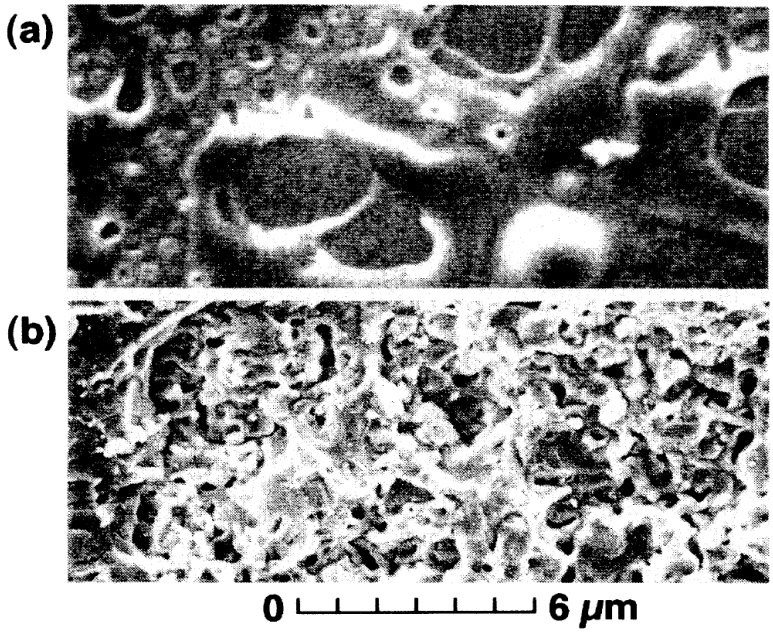

Figure 2.3: 1053nm pulsed laser damage of fused silica. (a) Thermal damage from 900 ps pulses showing melting, (b) Fracture and ablation without melting for the shorter 500 fs pulse. Figure from [1]

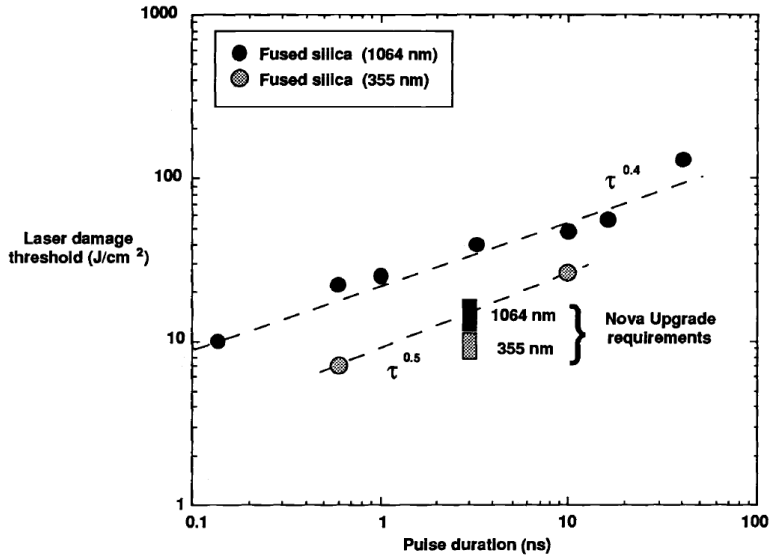

Figure 2.4: Pulsed LIDT's of fused silica from LLNL's NOVA laser program [8]. An approximate $\tau^{1/2}$ dependence of the thresholds originates from the damage caused by thermal buildup and melting of the material.

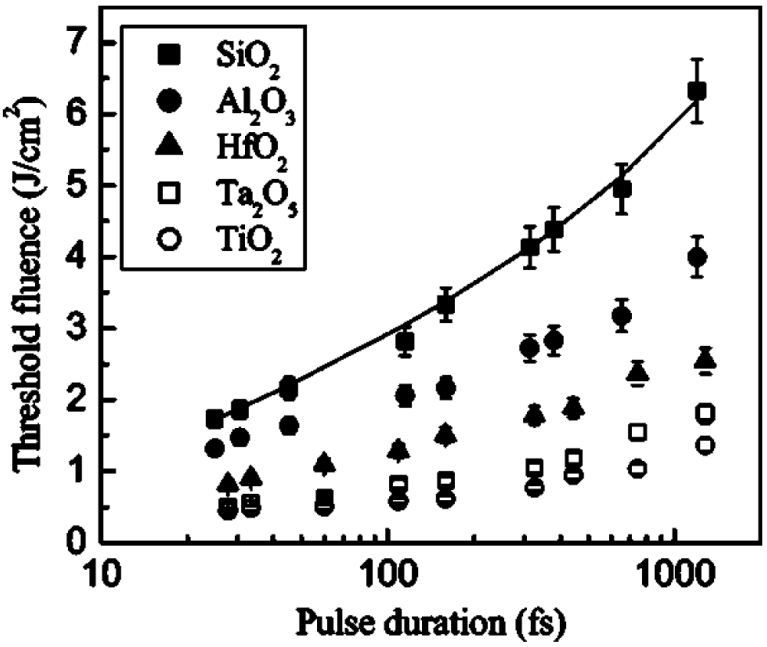

Figure 2.5: Pulsed LIDTs of materials with differing bandgaps. Notice the increasing damage thresholds with larger bandgaps from 3.3 eV titania to 8.3 eV silica. Figure from [3]

the focusing power of the thermal lens. This process can occur for pulsed lasers as well as CW.

2.3 Continuous-Wave Laser Damage

Continuous-Wave (CW) laser damage of optics has been an area of research for several decades, though smaller than the field of pulsed damage. The development of extremely powerful chemical lasers in the 1970's and 1980's drove early research. Chemical lasers derive their lasing energy from an exothermic chemical reaction, often running hydrogen fluoride or deuterium fluoride. This violent reaction excites molecules into upper lasing levels, creating a populating inversion necessary for lasing. Power levels of hundreds-of-kilowatts to megawatts (ABL and MIRACL) were achieved using this method, though at the cost of very large laser systems, toxic chemicals both before and after the reaction, expensive and limited laser runtimes, and a high temperature rocket-like exhaust plume leaving the system. The difficulty and expense of chemical lasers severely restricted research to just a handful of defense projects. When optics were damaged during testing it represented a significant expense and delay to the program. Expensive testing also limited the number of laser shots, making statistical analysis difficult and preventing separate research projects focused solely on laser induced breakdown. Though some chemical lasers have recently been investigated and fielded (THEL), most research has moved to smaller, more efficient solid state and fiber lasers.

Studies to model CW laser damage were prompted by these expensive failures and limited testing opportunities. Initial models of CW laser damage simply solved the heat transfer for an object with a given absorption and beam profile [9]. The lower the absorption and the greater the thermal conductivity of the substrate, the better the optic was expected to preform. Keeping the optic cool had the added benefit of reducing overall optical distortion associated with physical deformation of the optic from unequal thermal expansion, made worse by differing materials, and the changing refractive indices with temperature for dielectrics. Mirrors were often evaporated onto a thick copper substrate with cooling channels for a liquid coolant to reduce overall heating [10], see figure 2.6.

More recently, better coating techniques, specifically ion beam sputtering (IBS) have

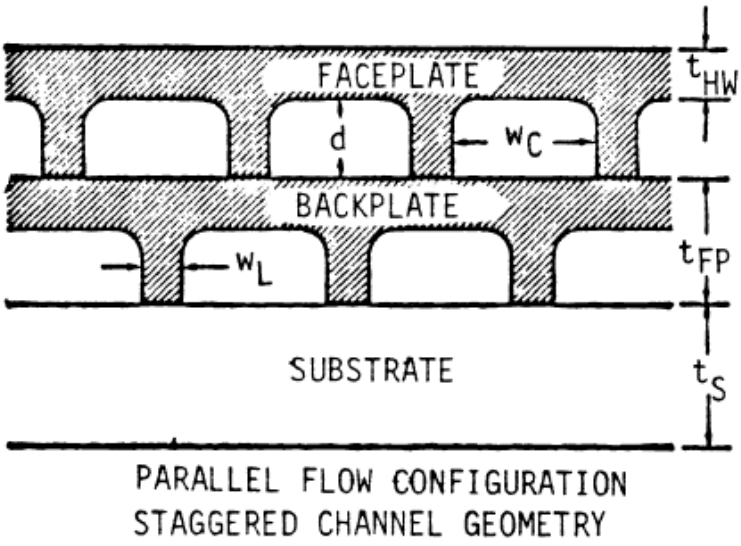

Figure 2.6: Coolant flow channels underneath the optical surface of an early high power mirror. Coolant channels are stacked to increase fluid flow and further reduce heating. Figure from [9]

largely replaced cooled metallic mirrors for high power applications. IBS coatings are fabricated by bombarding a sputtering target with a neutral ion beam. The sputtered atoms then impinge on the substrate to be coated with significant kinetic energy, forming a hard, dense film [11]. IBS coatings have very low intrinsic absorption and their dense nature makes them less susceptible to changing optical properties due to temperature, pressure, and humidity variations [12]. Electron beam and atomic layer deposition (ALD) have also been utilized for coatings. E-beam coatings have advantages in the speed of deposition and lower stress but produce more porous films, allowing water inside the coating, changing its refractive index. E-beam coatings also tend to have higher absorption and lower overall damage thresholds. ALD films are deposited by independently introducing two precursors (typically a metal-organic and water) into a chamber, completely purging the system between the gases to avoid mixing. Each precursor reacts with the substrate in a self limited reaction, providing precise control of total film thickness; however this also makes it the slowest deposition technique. Each cycle of the two precursors should yield an atomic monolayer, though in practice the

large size of the ligands of the metal-organic precursor causes some reaction sites to be obscured in a process known as steric hindrance [13, 14], making ALD deposition even slower. ALD films also tend to exhibit reduced damage threshold compared to IBS [11]. The dense nature and precise thickness control of ALD films means that they could still be useful for capping layers even if they are not suitable for the bulk of an optical coating.

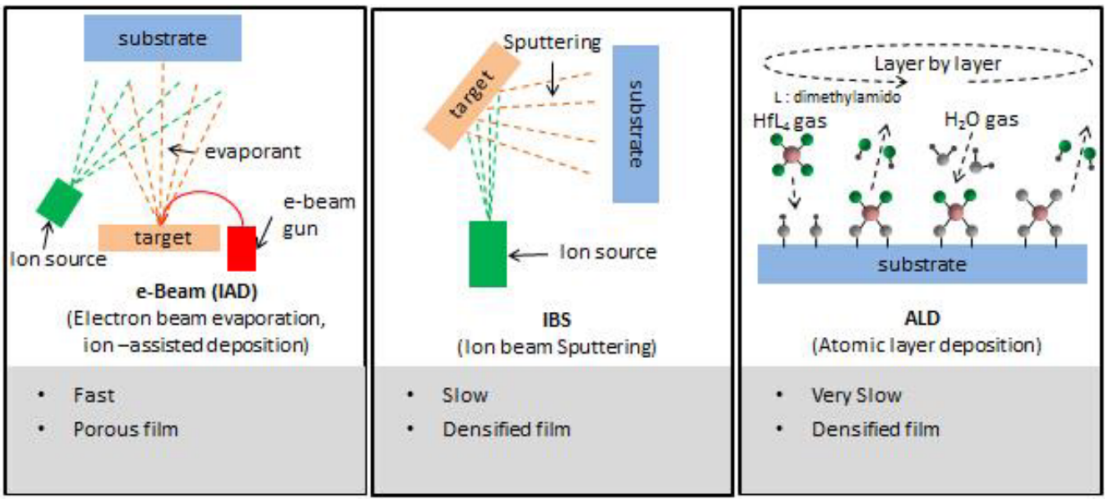

Figure 2.7: From left to right, E-beam, Ion Beam Sputtered (IBS), and ALD film deposition techniques. Figure from [11]

State-of-the-art IBS coatings can now be manufactured with extremely low absorption from tens of ppm to under 1 ppm. Rather than actively cooling optics, with such coatings heat is never absorbed in the first place, preventing the optical issues associated with thermal expansion and a changing index with temperature. Many coatings used for high power applications are reflective as they have less light interaction than a transmissive sample, reducing opportunities for absorption. Very high reflectivities are achieved by stacking quarter-wave layers of alternating high and low index materials in a structure known as a distributed Bragg reflector (DBR). These stacks can be upwards of 100 layers and several tens of microns thick, making stress control during deposition and proper annealing afterwards vital. Pristine IBS DBRs are capable of surviving mamy MWcm^{-2}, and are usually adequate for current CW laser system. With performance

of this level it would seem that CW laser damage should no longer be of concern. Unfortunately it was quickly recognized that some optics fail in a seemly random fashion and at far lower irradiances than expected. For a coating near single ppm absorption, such little power is absorbed that significant heat is not transfered into the optic and thermal damage cannot occur. Irradiances are also too low for non-linear and high field effects that cause pulsed breakdown to contribute. Clearly another mechanism must be in play for damage to occur.

Defects within the coating or contamination on the surface were quickly theorized to initiate the damage process. Experiments with pulsed lasers show significant reductions in damage thresholds for samples with surface contamination [15, 16]. Although care must be taken in extrapolating these results to the CW regime, similar results were observed during the development of high power CW lasers that were troubled by defects and contamination causing failures [17, 18, 9].

The exact mechanisms and series of events leading to defect/particle induced laser breakdown are still not certain. The most basic way a defect or contaminant can seed damage is by increasing the absorption of the material so that localized melting can occur at that point. Often a defect or surface particle is not observed until a test has started, though thermal images of the surface during exposure can easily identify the absorption centers as hot spots against a cool background [17]. Highly absorbing particles on a low absorption film also create large variations in temperature across the surface of the optic. These temperature differences cause unequal thermal expansion and stress within the multilayer film coating. Thick DBR coatings, even when designed correctly, already have residual stress between compressive and tensile layers. Thermal expansion in the plane of the film adds another stress component that can lead to the film layers cracking and delaminating [19]. If the heating is rapid enough, thermal shock will also contributing to film breakage. Often an audible "snap" can be heard when an optic fails quickly after a laser is turned on. Plasma formation is another mechanism thought to cause damage. The evaporating vapor from ablating surface particles can absorb additional laser energy to form a plasma. The plasma can contribute to heating, etching the surface, or in the case of oblique incidence add recoil momentum to the particle, causing thermal shock in the plane of the film [16], see figure 2.8.

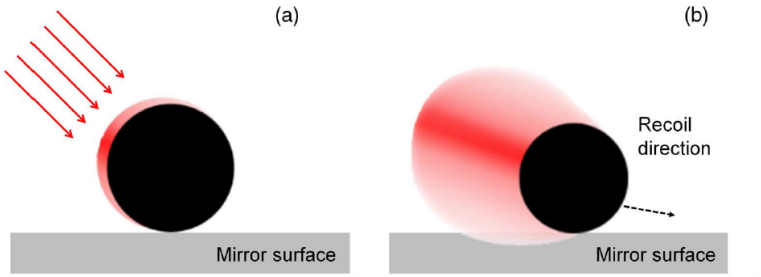

Figure 2.8: Plasma formation from heated sublimating particle vapor leading to a horizontal momentum transfer and surface etching. Figure from [16]

Regardless of what mechanism actually initiates damage, the thermal contact conductance between the particle and surface plays a key role in determining whether significant heat is transfered into the film or whether the particle can quickly evaporate away, leaving little damage behind. There are numerous reports of lasers actually cleaning the surface of coatings, reducing absorption and increasing damage thresholds [18]. Films with defects also show a marked improvement after laser conditioning [20]. Most intentional laser cleaning is done with pulsed sources, the on/off cycle causing the surface to expand and contract, "bouncing" the particle off. Adding a thin liquid (usually water) layer adds a vaporization force (steam cleaning) that helps eject particles [21, 22, 23, 24]. Though not ideal for the task, CW lasers also remove particles and condition surfaces, but there is a danger that too high of an irradiance will cause actual damage.

The following chapter details our early experiments and observations with particle induced laser damage. The results from these tests form the basis of our work on the band gap dependence of particle-induced CW laser damage and CW laser conditioning.

Chapter 3

Laser Damage Testing: Initial Experiments

3.1 Experimental Set-Up

Testing optics for their ability to survive laser damage requires exposing them to a wavelength of interest and increasing the irradiance until failure occurs. This requires a laser at the correct wavelength with enough power to damage the samples. Near IR, specifically 1064-1070 nm, is a popular wavelength range for continuous-wave (CW) due to good atmospheric transmission, the ability to use traditional optical materials (BK7, fused silica, ULE), and efficient Neodymium and Ytterbium doped lasers. While plenty of lasers exist in this wavelength range, getting enough power to damage samples is more difficult. Low power can, to a certain extent, be overcome by focusing the laser to a smaller spot, but this is at the expense of sampling a smaller fraction of the optic's surface. Since CW laser damage can be highly dependent on contamination and defects, decreasing the spot size reduces the number of particles or defects illuminated in a given test. The laser spot can easily miss particles or only illuminate a particle with the lower irradiance edge of the beam. This causes wide variations in the measured damage thresholds. Smaller beam spots also make characterizing damage morphology more difficult. A high power laser with a larger spot size eliminates these problems and effectively averages out any local contamination density variations. Because of these advantages, we heavily utilized a kilowatt class high power laser at Penn State's

Electro-Optics Center (EOC).

Laser damage testing conducted at the EOC used a 17 kW CW Ytterbium Doped IPG Photonics YLS-1700 fiber laser at 1070 nm. The output of the laser was approximately Gaussian with an M^2 less than 6, and was focused to produce spot sizes varying from 400 μm to 4 mm depending on the required irradiance, though the majority of testing occurred at 1 mm as this provided a large illuminated spot yet still allowed irradiances ranging from 60 kWcm^{-2} to 3 MWcm^{-2}. The laser power, beam size and beam shape were measured using a Primes PM100 power meter and a Primes FM120 focus monitor. Graphite blocks were carefully arranged to catch all the reflected and transmitted light off the sample though they have since been phased out as they tend to outgas and emit airborne particulates when strongly heated (it was common for the center of the beam dumps to be heated to yellow/white hot during testing at full power). This was mitigated with a large vacuum system that continuously removed the contaminated air. The laser was fired remotely from the adjacent room, protected by OD absorbing filters over the windows, see figure 3.1.

Some early tests exposed samples for up to 2 minutes. This was later shortened to 30 seconds and eventually to 10 seconds as damage always occurred nearly instantaneously to human perception. The sole exception to this in hundreds of shots of testing was when a large airborne particle was seen to settle on an optic several seconds into testing. Failure occurred immediately upon the particle reaching the optic's surface. When damage occurred during testing the laser was shut off manually to prevent further damage to the sample as the laser quickly began boring a hole through the substrate, reaching a depth of several millimeters in less than a second. The aluminum optical mount also could be melted if light scattered off the damaged sample, see figure 3.2.

The temperature at the surface of the optic was measured during laser irradiation using a thermal camera with a range 0-250 ^{o}C at 30 Hz. The spatial resolution of the thermal camera was approximately 1 mm. The maximum pixel temperature was used to measure the temperature within the 1 mm beam spot. Temperatures measured were an average of the optic's surface and any contamination. The temperature resolution of the thermal camera was a tenth of a degree Kelvin. The optics tested are near perfect blackbodies in the thermal IR so camera error due to emissivity differences was minimal. To examine the surface and contamination where the laser impinged, microscope images

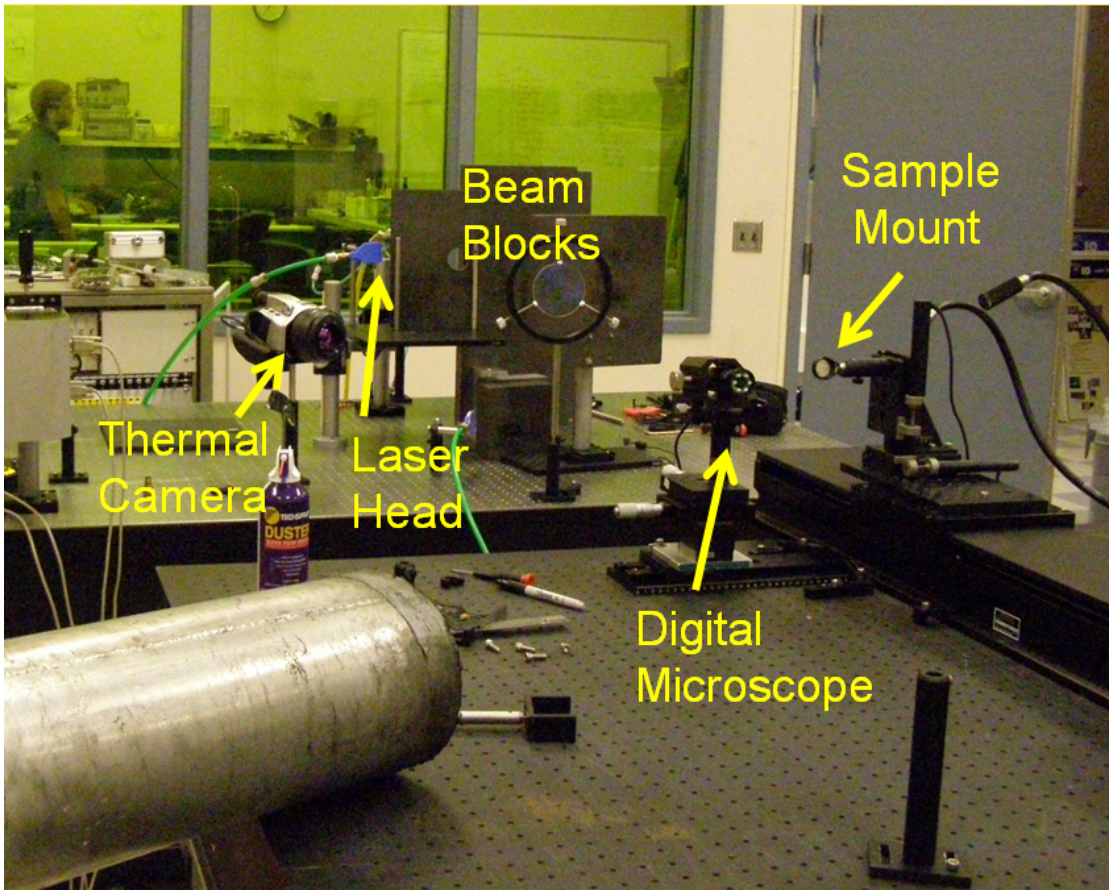

Figure 3.1: Laser damage test setup at Penn State's Electo-Optics Center. A thermal camera was used to take surface temperature measurements during testing and a digital microscope took before and after images of the surface. Graphite beam dumps are used to absorb stray laser power. The large silver cylinder in the lower left is the air intake of the vacuum system used to remove contaminated air from near the sample.

Figure 3.2: Damaged optic and its melted aluminum mount with an undamaged mount for comparison. The silica substrate, besides having a deep hole at the laser spot, is relatively undamaged.

of the optic were collected before and after each laser shot using a 200x USB Digital Microscope. A sliding dovetail rail with a stop allowed the camera to be easily moved in and out of position for each shot.

3.2 Samples Tested

The optics tested were IBS high-reflectivity distributed Bragg reflectors (DBRs) fabricated by ATFilms on 1" fused silica substrates, see figure 3.3. Both hafnia-silica (HfO_2-SiO_2) and tantala-silica ($Ta2O_2$-SiO_2) DBRs were tested. The hafnia-silica DBRs consisted of 89 layers with the top and bottom being silica. Tantala-silica DBRs consisted of 40 layers, the bottom layer being silica and the top Tantala. The DBRs were optimized for maximum reflectivity at 1064 nm. The absorption of the DBRs was measured using Photo Thermal Common-Path Interferometry (PCI). Hafnia-silica samples were measured at less than 7 ppm, and tantala-silica at less than 1 ppm.

Our first laser damage studies used optics contaminated with gold and silica particles. Most of the incident laser power was reflected or scattered from the surface with relatively little heating or change to the damage thresholds of the optics. The scattering was observed to heat the aluminum optical mount by a greater amount than the surface heating caused by the absorption of the actual laser spot on the surface of the optic, see figure 3.4.

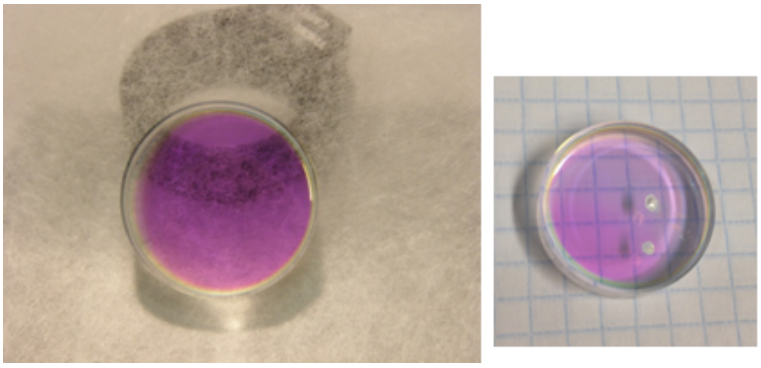

Figure 3.3: Left: Pristine hafnia-silica DBR on a 1" fused silica substrate. Right: Typical damage resulting from particle induced laser damage

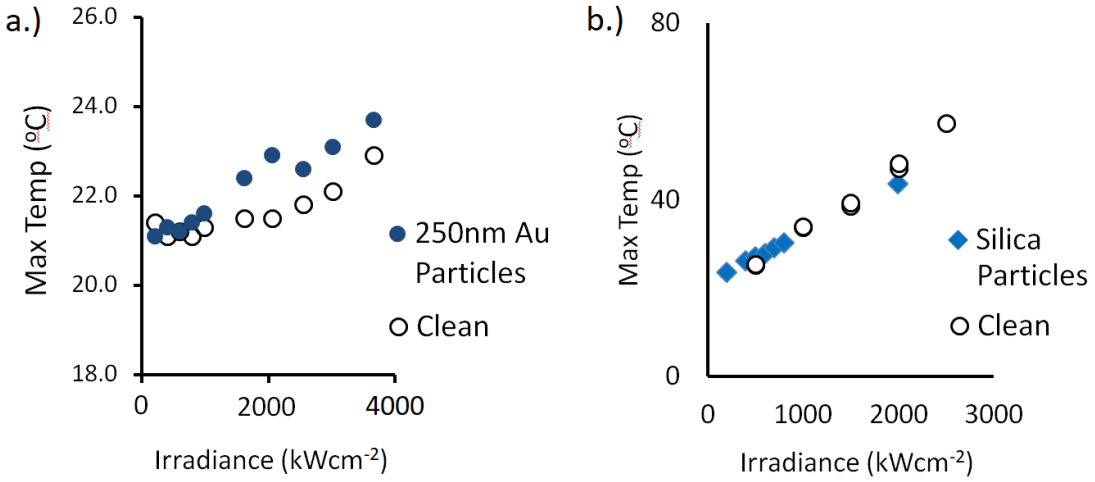

Figure 3.4: Maximum sample temperature during laser exposure of (a) 1 μm silica particles and (b) 250 nm gold particles.

To test effects of an absorbing contaminant, samples were intentionally contaminated with carbon microparticles. Carbon was selected to simulate real world contaminants due to its large absorption, high sublimation temperature, and prevalence in organics, such as green seawater. To contaminate the samples, pure carbon powder from SkySpring Nanomaterials, Inc. was mixed into a dilute solution with isopropyl alcohol (IPA) (0.07 g/mL) and dripped onto the optic until the entire surface was covered. The particles were allowed to settle for two minutes, and then the excess was blown off the surface with compressed nitrogen. Blowing the surface off before the alcohol was allowed to fully evaporate prevents particles from agglomerating. The particles used were labeled as 20-50 μm, however measuring the particles using laser diffraction (Microtrac S3500) found the average particle size to be 7 μm, with 5th and 95th percentiles being 4.2 μm and 19.4 μm respectively. The density of particles varied across each optic with an average density of 130 particles per square millimeter, though this could vary significantly location to location, see figure 3.5. The absorption measured with PCI after carbon contamination was several thousand to several tens of thousands of ppm.

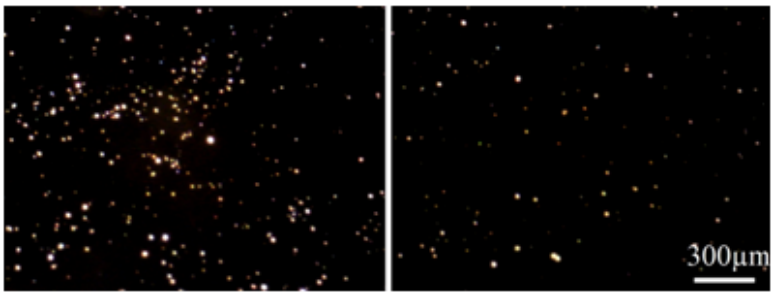

Figure 3.5: Microscope images of two carbon contaminated sample locations showing typical differences in contamination density across an optic's surface. The scattered illumination light off the particles cause them to appear white.

To maximize the use of samples, up to nine and in some cases 12 locations per 1" sample were tested. These locations were spaced 4 mm apart to prevent any crossover effects from other tests. If however a sample was damaged and it appeared that the other sites may have been contaminated from debris ejected from the damage area, the sample was retired from further testing. Locations were not reused for multiple shots unless specifically to examine conditioning effects due to previous laser irradiation.

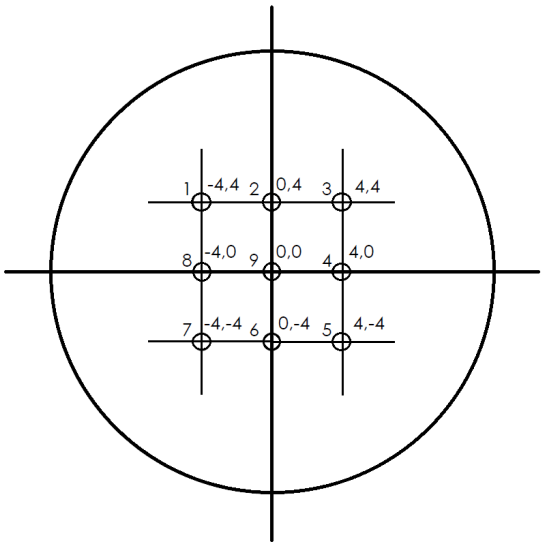

Figure 3.6: Laser test pattern used to maximize the use of samples while preventing any crossover effects from previous tests.

3.3 Test Results

The carbon contaminated DBRs were tested over a range of irradiances while surface temperature was measured. In every case, the samples contaminated with carbon experienced greater heating than clean samples for a given irradiance, as seen in figure 3.7. This was to be expected given the added absorption of the optic due to the carbon's presence. In general, higher irradiances caused greater sample heating, although location to location variations in the amount of carbon present on the surface affected this. A visible flash of light could be seen coming from the surface of the optic during the first instant of laser exposure. This was not visible for repeat shots at the same location. A spectrometer was used to measure the emission from the flash, see figure 3.8. Originally it was hoped that the flash spectrum could be fit to a blackbody curve or a molecular absorption peak, however the spectrum varied significantly flash to flash.

To verify that the differences in temperatures of contaminated optics were due to the density of contamination, contaminated samples were tested at multiple locations then cleaned via drag wiping using isopropyl alcohol to remove most of the contaminants. Figure 3.9 shows microscope images of an optic's surface before and after this cleaning.

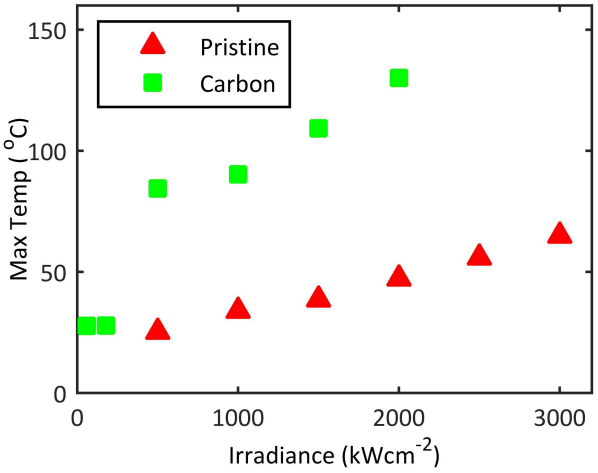

Figure 3.7: Maximum sample surface temperatures for pristine and carbon contaminated DBRs

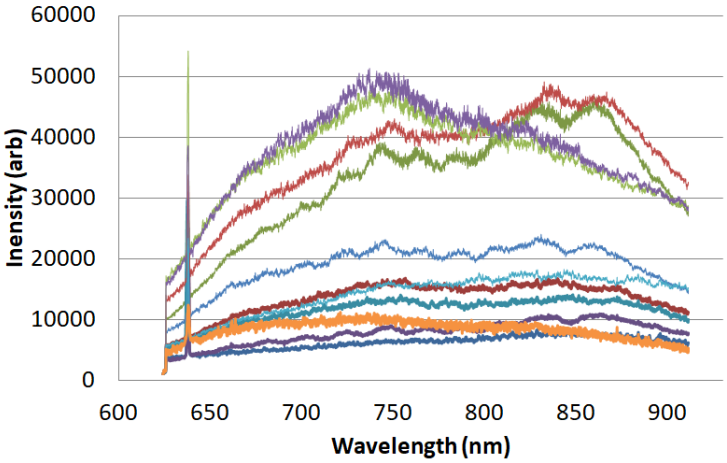

Figure 3.8: Spectra emitted from carbon contamination during initial laser exposure. Each series is a separate exposure of a contaminated region. The sharp peak is from a HeNe laser illuminating the sample

New locations on the cleaned samples were tested using the same irradiances. A large reduction in heating was noticed after cleaning, see figure 3.10

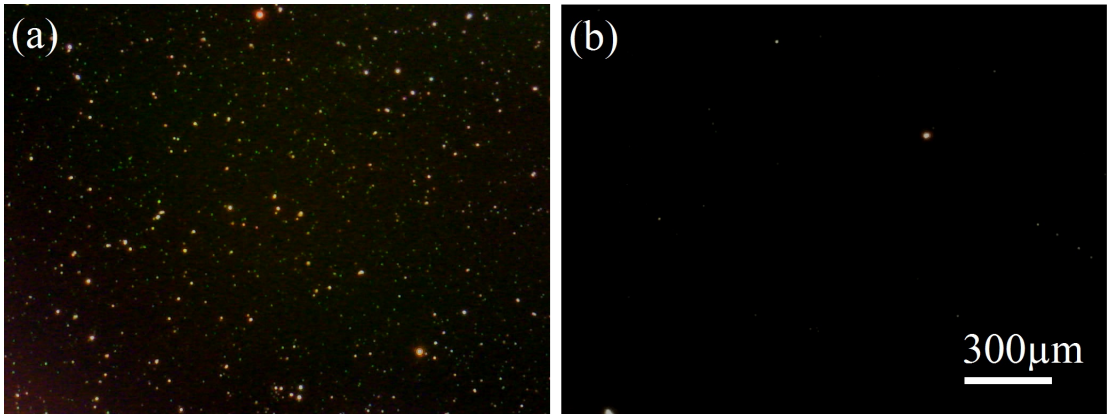

Figure 3.9: Microscope surface images of a carbon contaminated DBR (a) before and (b) after drag wiping with optics tissue and isopropyl alcohol

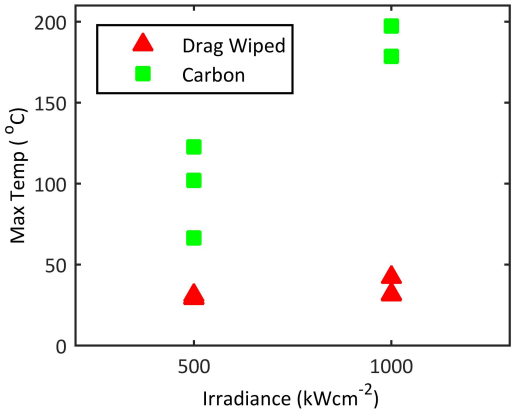

Figure 3.10: Maximum temperatures observed on contaminated and cleaned hafnia-silica DBRs. Freshly contaminated locations were tested and compared to tests of spots that had been contaminated then cleaned via drag wiping. The removal of most of the contaminants by drag wiping causes a large reduction in absorption and heating.

In addition to greater surface heating, failures occurred with contaminated optics that did not happen with pristine and drag wipe cleaned optics. Of the contaminated hafnia-silica DBRs, a single failure occurred at 1 $MWcm^{-2}$ out of 8 exposures. Other testing locations on multiple samples survived as high as 3 $MWcm^{-2}$. Tantala-silica

DBRs had a far lower contaminated damage threshold, with the lowest failing at 60 $kWcm^{-2}$ and 80% failing by 180 $kWcm^{-2}$. No pristine DBRs of either type were damaged during the course of testing despite being irradiated up to 3 $MWcm^{-2}$. Optics that had been drag wiped showed similar damage resistance to those of pristine optics. No tantalia-silica DBRs that had been cleaned failed despite being tested at 180 $kWcm^{-2}$.

The greatly reduced damage threshold of contaminated tantala-silica is in contrast with observed heating and absorption of the pristine films. In testing at 3 $MWcm^{-2}$ hafnia-silica DBRs experienced heating of 42.6 ^{o}C while tantala-silica DBRs only heated 1.2 ^{o}C. It is for this very reason that tantala films have typically been preferred over hafnia for many high power applications, their absorption generally being an order of magnitude lower, limiting heating and optical distortion. The damage results from these tests indicate that this conventional wisdom should be re-evaluated if contamination the optical system in question is possible. At this point in the study it was premature to hypothesis as to why the tantala-silica DBRs preformed so poorly though we noted that tantala has a significantly smaller bandgap relative to hafnia which provided a starting point for future investigations, see chapter 5.

Many high power optics use silicon substrates as its greater thermal conductivity helps to dissipate heat from absorption. Several DBRs on silicon with were tested and they demonstrated significantly less localized heating than the samples on fused silica. This was true for both pristine and carbon contaminated samples. One downside to silicon substrates was that when damage to the DBR occurred, the silicon substrate strongly absorbed the 1064 nm light, causing significantly more damage to the surrounding areas.

To test for conditioning effects, samples were tested twice at the same location and irradiance, and the two shots compared. This was done for both hafnia-silica and tantala-silica DBRs over a range of irradiances, but below the damage thresholds of each. A reduction in surface heating from the first to second shot was immediately apparent for contaminated samples seen in figure 3.11, showing the absorption of the sample had decreased from the first shot. This heating reduction was not present when clean optics were tested, implying that conditioning was affecting the particles, and not the films.

Reduction in heating due to sample conditioning was also noticed in the temperature

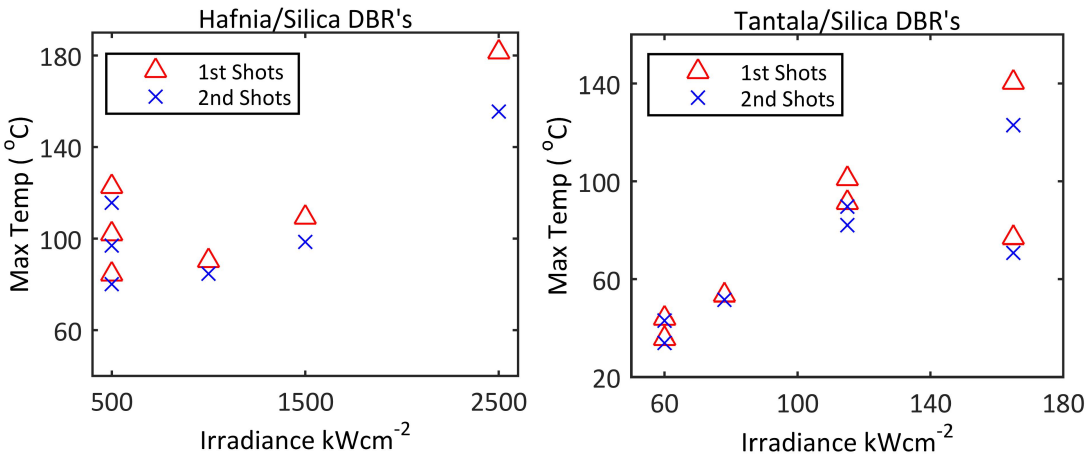

Figure 3.11: Maximum surface temperatures during 1st and 2nd 30 second laser exposures of carbon contaminated hafnia-silica and tantala-silica DBRs. Note the reduction in temperature between first and second shots as well as greater reductions occurring at higher irradiances.

vs. time profiles collected during testing. Freshly contaminated samples would often reach an initial high temperature and then begin to cool towards a lower steady state value, all while constantly being irradiated. Conditioning occurred within the first moment of the test, reduced absorption and allowed the optic to stabilize at a new reduced temperature. Figure 3.12 shows that optics conditioned at a higher irradiance exhibit a greater difference between the initial high peak temperature, and the conditioned steady state value. This real time heating reduction was not seen in subsequent shots of optics that had already been conditioned.

Conditioning was seen to have a strong effect on damage thresholds. A contaminated tantala-silica DBR was conditioned over a series of 9 shots to withstand 2 $MWcm^{-2}$ as compared to its normal first shot damage threshold of under 180 $kWcm^{-2}$. When damage did occur at 2.5 $MWcm^{-2}$, it was uniquely catastrophic with a 6-7mm area being blown out of the back surface of the substrate opposite to the normal surface crater at the front. In all the testing, no damage occurred at an irradiance that a sample had already once survived, further highlighting the effectiveness of conditioning.

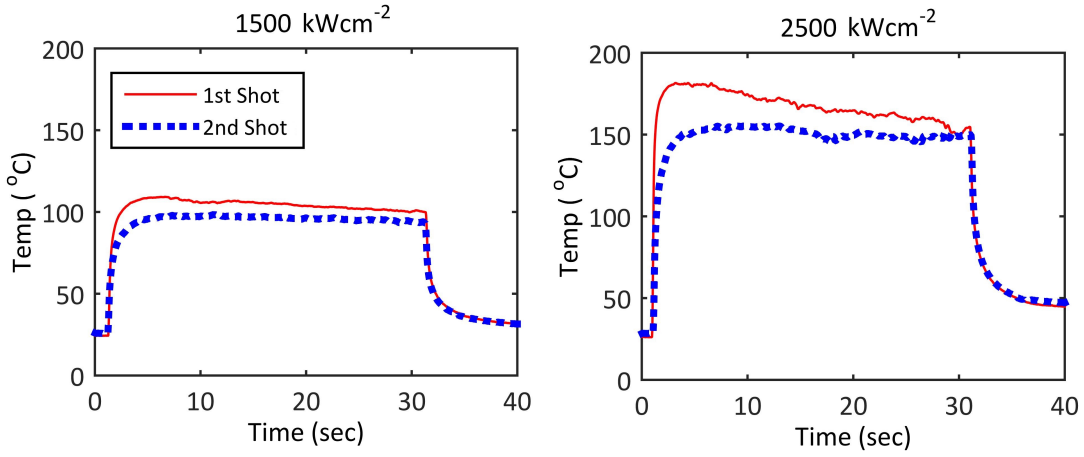

Figure 3.12: Temperature vs. Time of two repeat shots. Locations on carbon contaminated DBRs were tested twice at a given irradiance, and the surface temperature vs. time was recorded for both shots. First shots are seen to run at higher temperatures than second shots, particularly at the larger irradiance. Real time conditioning can be seen as the first shots reach an initial high temperature before conditioning reduces absorption and the optic begins to stabilize at a lower steady state value.

3.4 Particle Studies

Microscope surface images of the optics tested were taken before and after each laser shot. Changes in the position, size, and number of particles after exposure were noticed. When a sample was first exposed, many particles were removed from within the spot of the beam. The particles that remained were transformed and agglomerated within the beam spot seen in figure 3.13. To quantify this change, the images were analyzed using a MATLAB script. To identify particles, the images were converted to greyscale and a Sobel edge filter was used to highlight the particle edges, see figure 3.14(a) and 3.14(b). After the Sobel filter, the images have the rough outlines of the particles but with frequent small gaps, preventing the particles from being identified. To fill in the outlines, the images were morphologically closed (image dilatation followed by erosion) using an 8 pixel square, see figure 3.14(c). With the boarders of each particle clearly defined, they were then filled in to remove any holes and the area of the laser spot was highlighted with a mask, see figure 3.14(d). MATLAB was used to count and measure

each particle. The resulting data shows that virtually all particle removal/agglomeration occurred on the first shot, with subsequent shots causing little to no change as shown in figure 3.15.

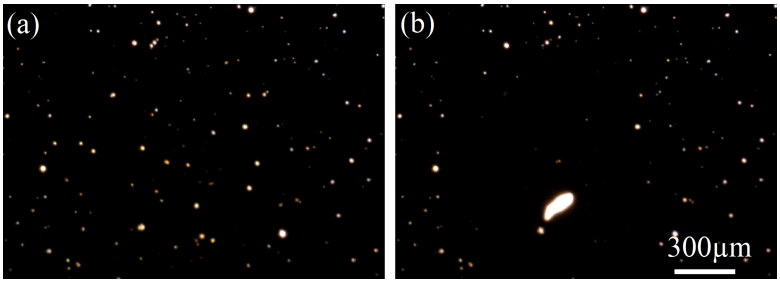

Figure 3.13: Images before (a) and after (b) laser conditioning. The circular pattern of particle removal with some newly formed large residue is typical of the carbon microparticle removal and agglomeration process seen.

To find the minimum irradiance required to transform particles, the surface images were used to find the radius at which particles ceased to be removed or agglomerated. This was compared to the beam profile of the laser so that the irradiance at each point in the image was known. For hafnia-silica samples the threshold was 17.7 kWcm^{-2} and for tantala-silica it was 15.1 kWcm^{-2}. Later experiments using PCI to measure absorption change found these values to be 11 kWcm^{-2} for the first observable change and 20 kWcm^{-2} to cause major conditioning, see chapter 4

Knowing that conditioning effects were occurring within the first moment of a laser shot, a high speed camera was used to film particles during their initial exposure. This testing was done at the University of Minnesota using a 175 W Nd: YAG laser with smaller spot sizes (200 μm) to produce similar irradiance levels to those used at Penn State's EOC. Particles were seen to brightly glow and move around the surface for up to 0.7 ms into the laser exposure, seen in still images taken from the high speed camera in figure 3.16. After this time the particles ceased to glow and had stabilized into their final agglomerated position. Particle motion appears to be random, although the limited number of camera frame capturing this motion makes it difficult to determine.

To test if contaminant mass was being evaporated off the surface, the volume of surface contaminants before and after laser irradiation was calculated using microscope surface images and surface profilometry. Images taken before testing were analyzed

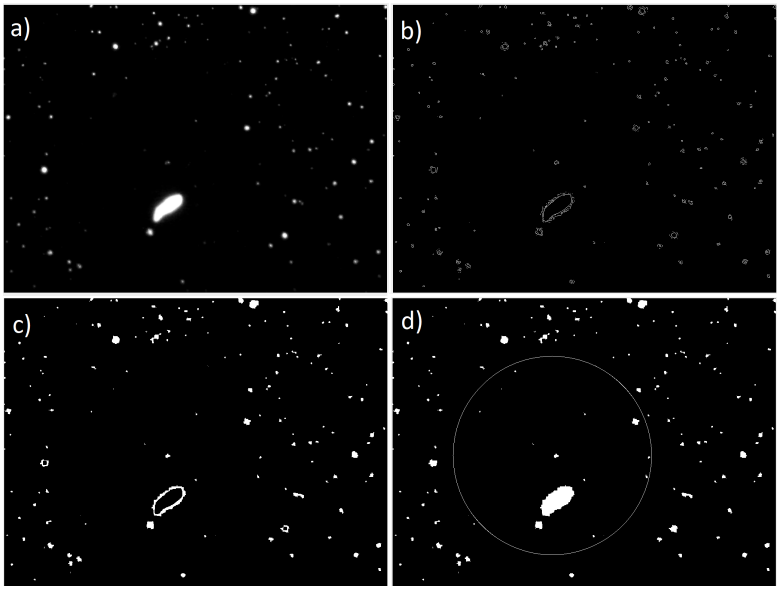

Figure 3.14: a) Greyscale surface image of carbon particles . b) Image after Sobel edge filter. The particles are clearly defined but small gaps exist in their outlines. c) Image after closing, the outlines are now complete. d) Image after filling in the particles and applying a mask around the laser beam area

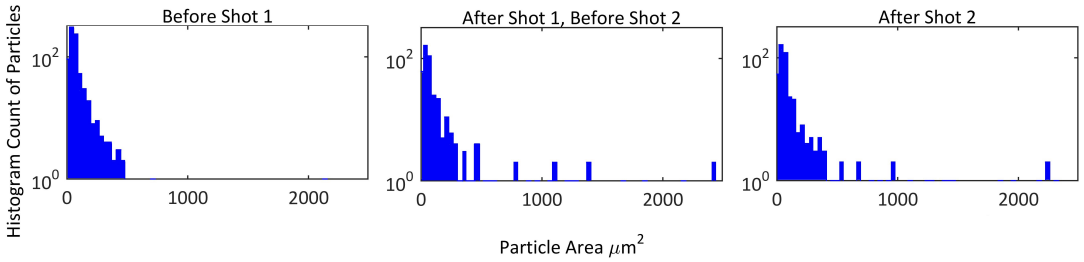

Figure 3.15: Total histogram counts of carbon microparticles from seven tests of two repeat laser shots. The number of small particles has decreased and large particles increased, corresponding to particle removal and agglomeration. Virtually all particle changes occur within the first test, the second test doing little to change the distribution.

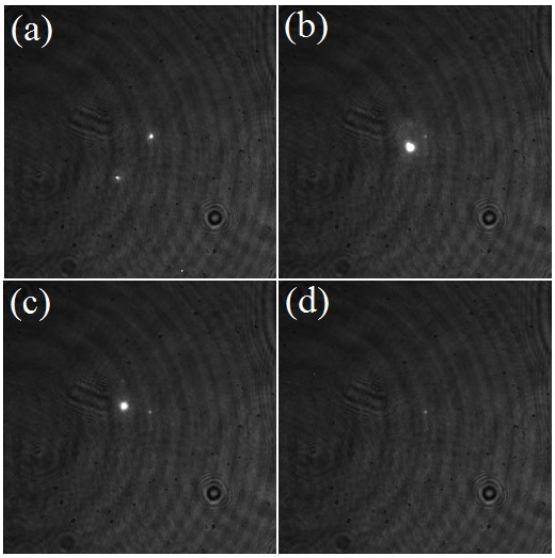

Figure 3.16: High speed photo images of the carbon particle conditioning process from top left: 0.17ms, top right: 0.24ms, bottom left: 0.6ms, bottom right: 0.76ms.

using the MATLAB script to count particles and measure their area. The volume of the particles was calculated from their area using a spherical approximation. This approximation was justified as the sphericity (ratio of the surface area of a perfect sphere to the surface area of the object) was measured at 89.5 % with a standard deviation of 6.7 % using a Microtrac Bluewave laser diffraction particle analyzer in the Minnesota Nano Center (MNC). After laser exposure, particles had drastically changed shape, flattening and broadening among other less consistent changes, and volume could not be determined from the after images taken.

To measure the final volume of particles, 3-D scans were taken using a P-16 surface profilometer, shown in figure 3.17, with data taken every 8 μm x 0.5 μm. Of the samples measured, the remaining volumes were all significantly reduced from the originals, with the remaining volumes varying between 3% and 76% of the originals. The residue was mechanically fixed to the surface and did not move from the 1 μN force exerted by the profilometer tip. Carbon particles that had not undergone conditioning were more weakly bonded to the surface and could be moved by the profilometer tip.

When viewed in a bright field microscope, the conditioned particles were noticed to

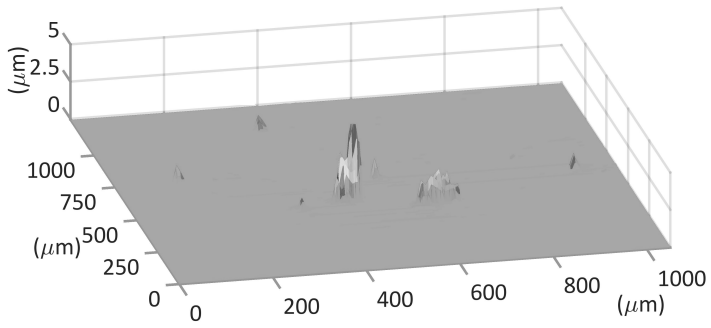

Figure 3.17: Surface profilometer scan of a conditioned optic with contaminant residue. The residue covers a wider, shallower area than the carbon particles before laser irradiation. Surface scans were used to calculate the final volume of contaminant residue after laser conditioning.

have changed transparency, seen in figure 3.18 To test for elemental changes, a conditioned sample was analyzed by two methods. Energy Dispersive X-ray Spectroscopy (EDS) was attempted but static charging from the electron gun of the scanning electron microscope (SEM) and the insulating nature of the sample prevented a clear image of the sample from being taken. Regions of interest could not be resolved so a new measuring technique was required. Time of Flight Secondary Ion Mass Spectroscopy (TOF-SIMS) was used. This measurement technique can analyze small areas allowing elemental composition of a specific region to be gathered. Regions of interest were selected via an optical microscope and could be clearly resolved. Conditioned spots were measured with a higher hydrocarbon signal in comparison to the pristine carbon particles, see figure 3.19. TOF-SIMS measurements were conducted by Evans Analytical Group.

To see if heating alone could cause similar particle transformation, pristine particles were heated in a rapid thermal annealing (RTA) system to 1100 ^{o}C to see if similar conditioning effects could be achieved. No such changes were measured, implying that the particles are reaching higher temperatures during testing. The white light observed being emitted by particles in the first moment of laser exposure is likely blackbody radiance, indicating that temperatures in the excess of 2000 K are being reached.

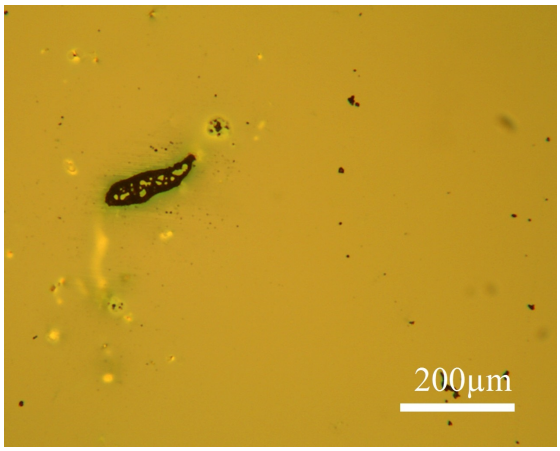

Figure 3.18: Pristine particles on the right and conditioned particles on the left. The transparency change of the particles is typical of all laser shots.

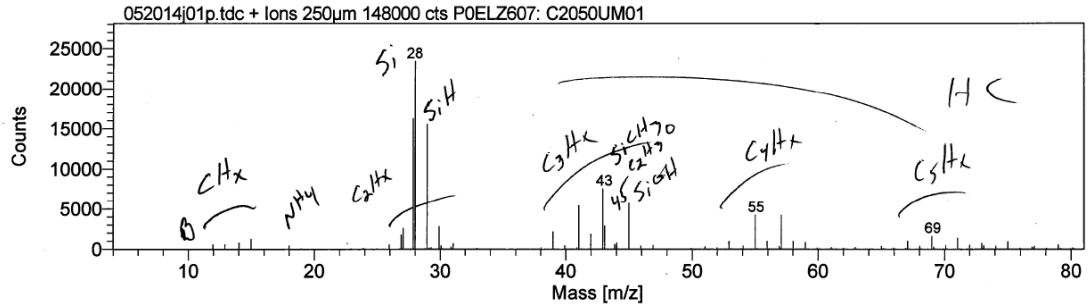

Figure 3.19: TOF-SIMS data of an area of residue after laser conditioning. Most peaks correspond to hydrocarbon molecules.

Chapter 4

Quantifying Laser Conditioning using PCI

4.1 Introduction

Although the exposure of contaminated optics to high irradiances often leads to catastrophic failure, lower irradiance exposure with pulsed sources have been reported to have a beneficial conditioning effect on optics [25], [20]. Laser cleaning, a closely related process, is a well established technique that utilizes a pulsed source to remove surface contamination [22, 23, 24] . Laser cleaning, and by extension, pulsed laser conditioning, removes contaminants by rapidly heating and cooling the area immediately underneath a particle. The mechanical strain and stored elastic energy caused by the thermal expansion and contraction of the substrate can overcome surface adhesion forces and bounce a particle off the surface [22], [23]. Liquid is often added to the surface to increase the lifting force on the particle in a form a steam cleaning [23]. Though useful for some applications, requiring a separate pulsed source to clean optics in a continuous-wave (CW) laser system is less than ideal. While careful contamination control and regular cleaning are the preferred methods to prevent laser damage, many situations require operation even when faced with random contaminants. A CW laser system that could self-clean and condition with a low power initial start-up shot would be highly desirable and add little to no cost.

CW laser conditioning has not been studied as extensively as its pulsed counterpart however numerous studies have qualitatively noticed conditioning's beneficial effect on damage thresholds [18]. The results of the our initial laser damage testing at Penn State's EOC confirmed these findings and demonstrated both reduced absorption/heating and increasing damage thresholds of particle contaminated optics, see chapter 3. To better understand the laser conditioning process, we set to find the irradiance and duration of exposure required to cause a reduction in absorption. With these values known, we can begin to model the physical processes at work in conditioning and determine the feasibility of using such process as a means of preventing laser damage.

4.2 Photo Thermal-Common Path Interferometry

To quantify the conditioning effect, a precise measurement of a sample's absorption before and after exposure was needed. Carbon contaminated samples had been previously measured for us by ATFilms using their photo thermal common-path interferometer (PCI). As part of our (JTO-ONR) research grant we were able to buy a similar system from Stanford Photo-Thermal Solutions and install it in our main lab in Minnesota, figure 4.1.

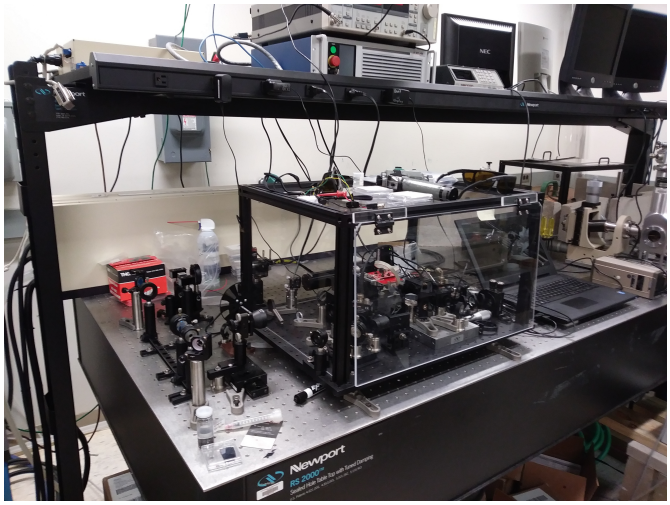

Figure 4.1: Photo thermal common-path interferometer at the University of Minnesota

PCI measures a sample's absorption by locally heating a region of interest with a

chopped high power CW pump laser and using a second low power probe laser to detect an intensity change at the frequency of the chopper [26]. When a sample is heated by the pump, the optical path length in the region changes depending on the thermal expansion and the dn/dT of the material. This change is periodic at the chopper's frequency. The probe beam is much larger than the pump, so only the small center region of the beam experiences a phase shift from the heated region. The phase change effectively creates overlapping two beams, the original large diameter beam, and a slightly phase shifted, much smaller beam in the center. The original beam's large waist compared to the shifted beam's smaller diameter allows the original beam to be treated as a plane wave while the small beam acts as a quickly diverging Gaussian. Due to the Gouy phase shift, after the two beams have propagated a distance z together, the difference in phase between them will be $\theta_G(z) = -arctan(z/z_R)$, where z_R is the Rayleigh length. This phase difference causes interference, periodically attenuating the overall power of the combined beams at the frequency of the chopper, see figure 4.2 This signal is measured using a detector and lock-in amplifier with the chopper as a reference for the lock-in. The use of a chopper and lock-in removes any signal not at the chopper's frequency, greatly reducing background noise and increasing sensitivity.

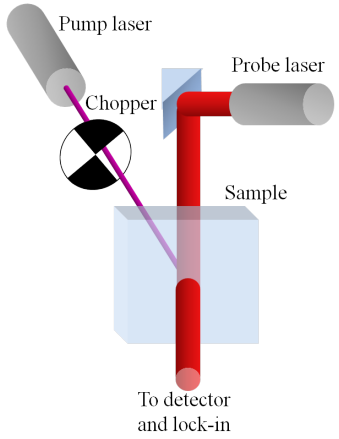

Figure 4.2: Basics of a PCI measurement. Pump heating of the sample creates a localized hot spot and phase change in the center region of the probe beam. After propagation a short distance, the two parts of the probe beam interfere to modulate the intensity, which is measured using a lock-in amplifier and detector

The pump laser determines the wavelength that will be measured as well as the

sensitivity of the overall measurement. Higher pump irradiance will increase the signal and allows for the measurement of very low absorption materials. In our case we opted to use an IPG photonic YLR-10-1064-LP Ytterbium doped fiber laser at 1064 nm and with 10 W of output power. The pump is linearly polarized, which though not required for PCI measurements, allows for an attenuating polarizer to easily fine tune low power levels used during calibration. After passing through the chopper, the pump is focused down to a small spot size in order to generate sufficient heating even in low absorption materials. At full power when focused to 56 μm the system is capable of making sub ppm absorption measurements. Filtering the lock-in signal increases the resolution down to 20 ppb but at the expense of much longer scan times. The pump spot size, in addition to determining the signal strength, also determines the spatial resolution of the system. Most measurements are taken using a 56 μm spot. A 5x beam expander before the focusing lens allows for the resolution to be increased to roughly 13 μm, though at this small of a spot the pump and probe more prone to drift out of alignment (this is made worse by mechanical slop in the adjustable lens of the beam expander) and calibrations have to be done several times daily. We originally planned on using our main 175 W Nd:Yag laser as the pump however its large M^2 would have required spatially filtering the output with a ceramic pinhole in order to get the desired beam quality and spot size. Furthermore as the laser is pumped by an older flash lamp (600+ hours) and each PCI surface scan can take several hours, it is very likely that the flash lamp would have burned out and replacing it would have cost as much if not more than the IPG fiber laser. Finally adjusting the output power of the fiber laser is easily done in an user interface while the Nd:Yag only has a coarse knob to adjust pump current. Needless to say, purchasing a dedicated pump fiber laser made working with the PCI system significantly easier.

The probe laser needs to have a stable Gaussian output. For our system we use a standard HeNe laser. For samples with transparent substrates (i.e fused silica, BK7, and ULE) the probe passes through the sample and is detected on the other side with a silicon photodetector. Samples that are not transparent to the HeNe (most commonly silicon substrates) reflect the probe beam and it is collected after the reflection. Transmissive and reflective refers to the probe wavelength, not the pump. The majority of the pump must either be reflected or transmitted through the sample otherwise the sample will

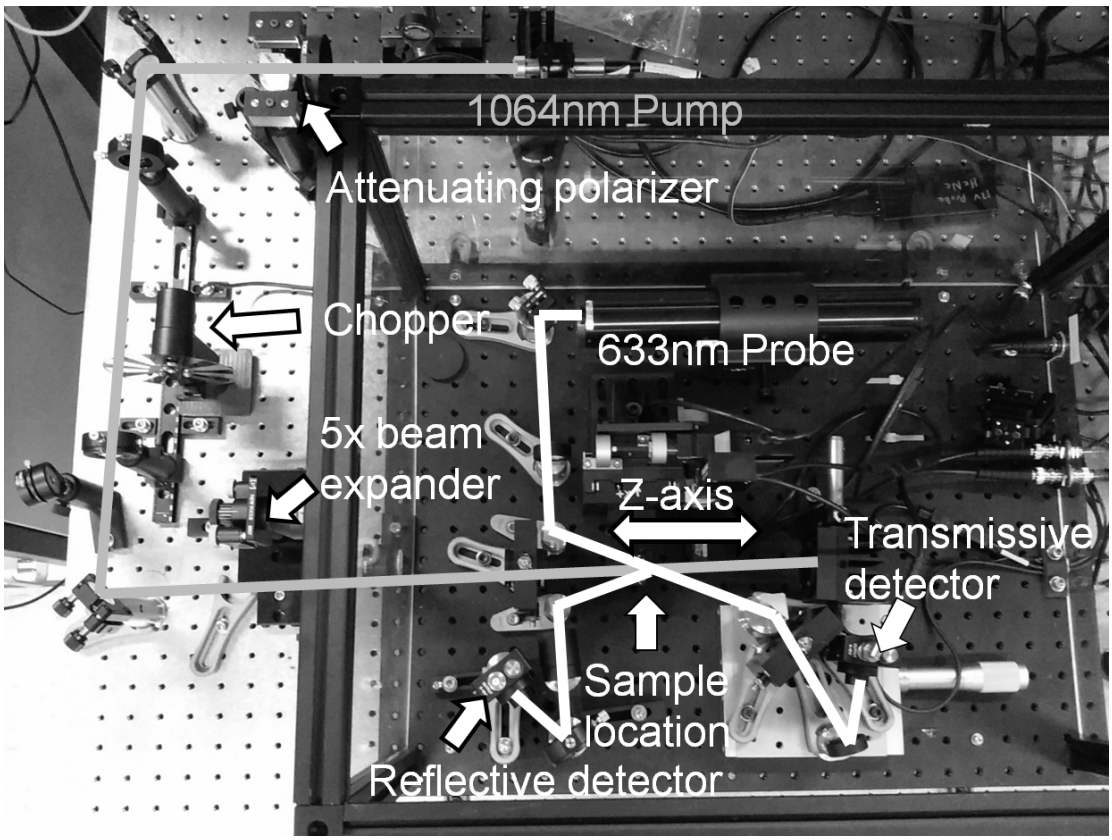

Figure 4.3: Beam paths and major components within the PCI system. Note both reflective and transmissive probe beam paths are shown. In practice only one is used at a time.

be damaged.

Measuring optical films requires finding the location of the pump/probe crossing on the surface of the sample. This involves scanning the optic through the z-axis of the system until the AC signal from the probe is maximized. For transmissive measurements this is relatively simple as the probe beam maintains its location on the detector regardless of the sample's position, allowing the sample to be scanned over a wide z range to find the surface. In reflection, the probe beam will move off the detector when the sample is moved, limiting z-scans to less than 0.3 mm before the probe beam needs to be readjusted. In practice the best way to overcome this is to use a transmissive sample with the same dimensions as the reflective sample. The approximate z location is found using a transmissive sample, the samples are swapped, then the surface's location is fine-tuned by testing near the approximate location, maximizing the probe DC signal at each point, and finding the z location with the largest AC probe signal. This in general makes reflective measurements significantly more difficult than transmissive.

To calculate the absorption from the raw AC probe signal, calibration of the PCI is required. To calibrate, a sample with known absorption and substrate (OD 0.2 filter on fused silica) is measured and the pump power, probe AC and DC signals are measured. This gives the responsivity of the system. From the responsivity the absorption of any other sample on a similar substrate can be measured. For samples with substrates that have different thermal conductivity, expansion, and dn/dT, multiplication by a correction factor accounts for the material differences, see equation 4.1. Since fused silica was used as the calibration sample, it has a correction factor of 1. Silicon with significantly higher thermal conductivity generates a much smaller PCI signal for the same absorption and has a correction factor of 22. If the film on the surface of the substrate is sufficiently thick (10's of μms) the material properties of the film become more important in the correction factor calculation and can mask the underlying substrate. This was observed in fused silica and silicon witness samples from the same IBS deposition run. When measured using the PCI, the difference in AC probe signal was only 2x between fused silica and silicon instead of 22 expected for a pure silicon sample.

$$Abs = CorrectionFactor * \frac{Probe_{AC} * \mathcal{R}}{Probe_{DC} * P_{Pump}} \tag{4.1}$$

4.3 Initial Conditioning Experiments

Carbon-contaminated hafnia-silica distribute Bragg reflectors (DBRs), like those used in the laser damage testing at the EOC, were exposed with our 175 W Nd:Yag laser and the surface measured to see if any conditioning could be observed. Extra heavy contamination was applied to aid in finding the exposed region when moving the sample from the laser into the PCI. The reduction in absorption due to the exposure was readily apparent with absorption dropping from over 20,000 ppm to less than a thousand, see figure 4.4.

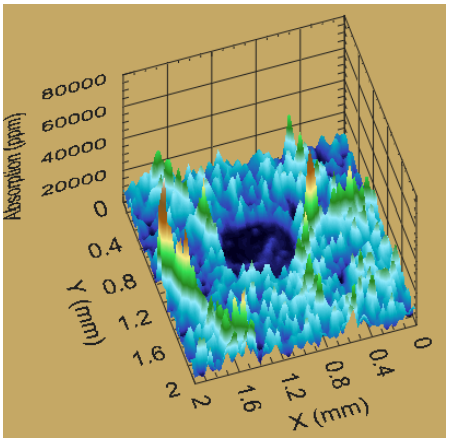

Figure 4.4: Area absorption scan of a heavily carbon contaminated hafnia-silica DBR. The central region has been exposed to approximately 25 kWcm^{-2} and a large reduction in absorption is apparent

With the basic principle and measurement known to be working, it was desired to get absorption data before and after laser conditioning. Moving samples into and out of the PCI to measure, condition, then remeasure, all at the exact same location, proved to be tedious. Seeking a better solution it was realized that the PCI's pump laser itself could be used to condition samples, removing the need to transfer samples into and out of the instrument. Surface scans of contaminated samples taken at high pump powers showed significant absorption reduction from the first to second scan, see figure 4.5. Increasing the pump power between scans further reduced absorption, see figure 4.6

Though useful for gathering qualitative information about conditioning, repeat area scans have several challenges that prevent quantitative conditioning measurements from

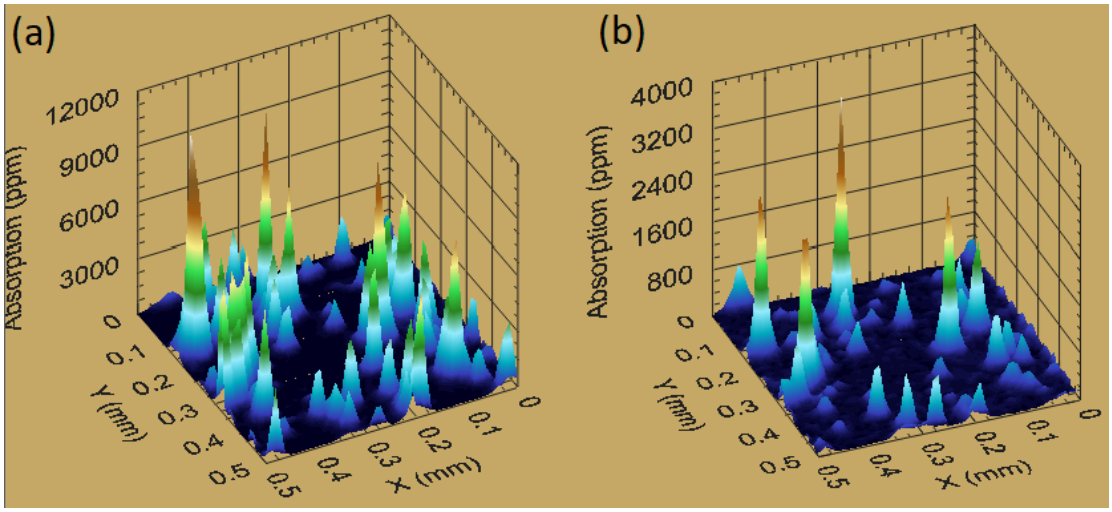

Figure 4.5: Repeat area scans of a carbon contaminated hafnia-silica DBR. Notice the reduction on absorption from the first scan (a) to the second scan (b). The absorption of some particles is reduced while others are removed completely.

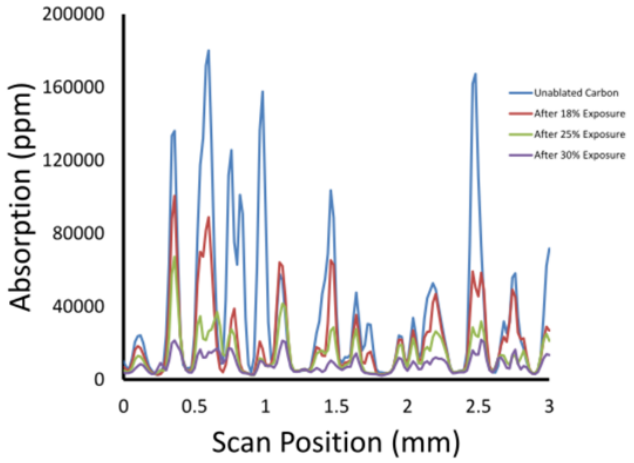

Figure 4.6: Repeat line scans with increasing irradiance of a carbon contaminated hafnia-silica DBR. By the final scan, absorption has been dramatically reduced.

being made. Conditioning occurs during the first measurement making the true initial value unknown. To prevent this, a low power initial measuring scan can be done followed by a high power raster to condition, and finally a follow up low power scan to measure the final absorption. This eliminates conditioning during the measurements however since the pump laser is rastered across the sample it can possibly be heating nearby regions and making the true exposure of a given area greater than what is expected. The limited scan speed also prevents exposures shorter than approximately 10 ms for a given region. Because of these complications alternative methods to measure conditioning were explored.

4.4 Conditioning Measured in Real Time

Though the simultaneous conditioning and measurement of a sample proved to be undesirable for area scans, it can be advantageous for single point measurements. If the absorption of a region is measured vs. time, any conditioning can be detected as a decrease in absorption, providing information about how much conditioning is occurring and over what timescale. Initial testing was done, measuring samples with a very low irradiance (3.6 $\mathrm{kWcm^{-2}}$), then stepping up the pump power and recording the AC probe signal strength over time, see figure 4.7(a). Using the calibration of the system to account for the change in pump power, the absorption was calculated, see figure 4.7(b). The low pump power used for the initial measurement was possible as the samples before conditioning had 1,000-10,000 ppm of absorption which gave sufficient PCI signal even at such low pumping.

At first glance the exponential decay of the absorption following each increase in pump power appears to give a conditioning time. However because the measurement was taken using a lock-in amplifier, the exponential decay is actually due to the time constant of the lock-in. For a rapidly changing signal a lock-in will take 5-6 time constants to adequately stabilize. The data was taken using a time constant of 100 ms, so any conditioning faster than half a second will not be accurately recorded. The obvious solution to this is to decrease the time constant of the lock-in, though this reduces the signal strength and increases noise as there are fewer cycles over which the amplifier integrates. To keep the same signal strength and allow for faster measurements

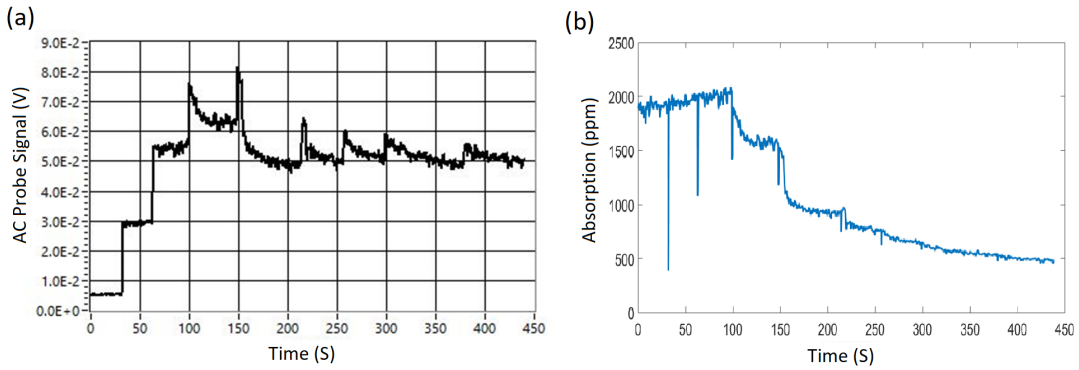

Figure 4.7: Real time conditioning and absorption measurement of a carbon contaminated DBR. The pump laser's power is increased in a series of steps and the probe's AC signal is measured, see (a). The absorption from the AC probe signal is calculated, taking into account the steps in pump power, see (b). The absorption is clearly seen to decrease in the fourth and fifth steps, then gradually stabilizes towards final value over the last several steps. The slight increase in absorption during the first three steps is likely due to particles heating up and thermally bonding with the surface, increasing the observed PCI signal.

the chopping frequency needs to be increased. A 60 slot chopper wheel was used and frequencies up to 1 kHz were tested. At higher frequencies the dynamic response of the system was improved however the system's responsivity was found to decrease when calibrating. The high chopping speed most likely limits the heating of the sample, reducing the observed AC probe signal.

Another complication with real time photo thermal common-path interferometry (PCI) conditioning measurements is that the pump is not strictly CW. Chopping the pump laser causes the sample to undergo alternating heating and cooling that it would not experience in a real laser system. One means of having a mostly DC conditioning beam but still being able to conduct a PCI measurement is to use a laser with a small AC signal riding on a large DC offset. The DC signal will condition the sample while the lock-in amplifier will be able to filter out the DC and amplify the AC signal for the PCI measurement. Any heating and cooling variation caused by the AC signal will be negligible compared to the large DC component. In principle this should work however modulating the pump laser requires an electro-optic modulator. The modulator and driving electronics needed to create large voltages across the modulator were deemed too

expensive. It is also possible to use two separate lasers for the DC and AC components, however aligning both with the probe beam and the sample would be very difficult, and physically fitting another laser in the system was not feasible.

4.5 Refining Contamination and PCI Measurement

A simple solution to the PCI measurement problem was found by conducting a low power initial measurement, briefly exposing the sample to a higher power without the chopper, then reducing the power and conducting a second measurement to find the absorption change. Although this method only tests a single exposure time per measurement, this eliminated the problems associated with surface scans and real time measurements. To control the exposure time, a function generator set to 'single pulse' mode was used to interface with the pump laser to turn it on and off. Initially this caused problems as the CW laser was not capable of turning on and off fast enough for the shorter pulses and the output of the laser varied wildly during start-up. This was solved by directly controlling the laser's pump current rather than issuing on-off commands. By controlling the current, the laser could be set to just below its lasing threshold for the off period and then to the desired power for the short pulse. Keeping the current just below threshold rather than completely off keeps many states in the laser excited and greatly helps to speed and smooth the turn on. Had this not worked, a fast mechanical shutter or electro optic modulator would have been required.

The earlier conditioning measurements, though qualitative, had revealed that the large variations in absorption across the surface of a sample could add unwanted variability in the experiments. Because of the limited spot size of the pump, large 20-50 μm particles used in the initial conditioning caused wide variations in measured absorption. Smaller graphite flakes were chosen for the new tests as they more evenly coated the optics and created less variations in absorption. A larger pump laser spot size of 110 μm was also used for the new measurements to capture the absorption of multiple graphite particles at each sample location, increasing the total number of particles surveyed, and further helping to average. The size and shape of the smaller particles were measured using optical and electron microscopes, see figure 4.8. Gold was evaporated on the sample to ground it and to prevent static charge build up from the e-beam of the SEM.

Individual particles were close to 1 μm in size though they formed agglomerates varying substantially from volumes of 1 μm on a side to over 10 μm on a side. Half the agglomerates were larger than 4 μm in at least one dimension with 10% being larger than 7.5 μm. With the graphite contamination, absorption values increased from single ppm to 1,000-10,000 ppm. A low pump power of 320 mW, yielding an average irradiance of 3.4 kWcm^{-2}, was used to prevent unintentional particle heating and conditioning during measurement. Locations tested were spaced apart by 300 μm to prevent any cross effects from neighboring locations.The substrate underlying the DBR coating was 6.35 mm of fused silica allowing for easy transmission of the probe laser. To find the conditioning threshold of particles under steady state conditions, long 1 second exposures were tested at different irradiances. Once a clear threshold was determined, shorter exposure times were tested at an irradiance above the long duration threshold to test for effects relating to the exposure time.

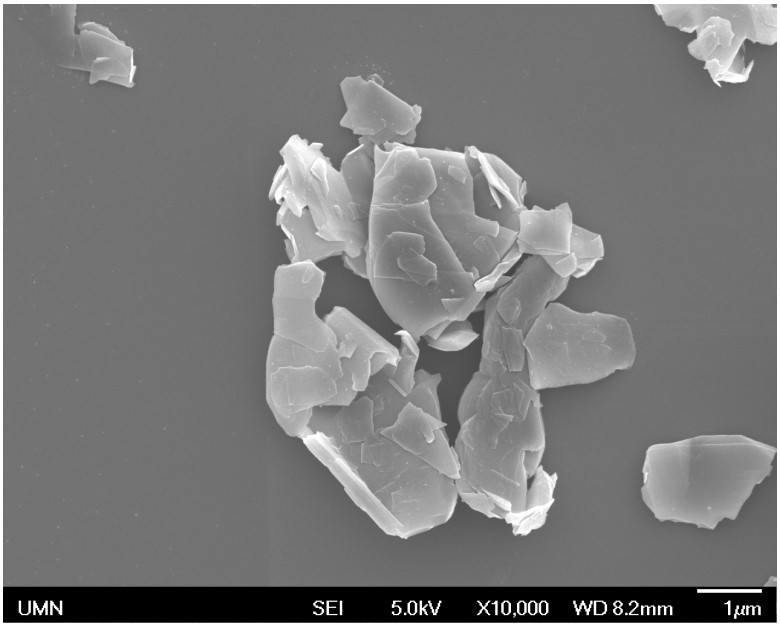

Figure 4.8: SEM of 1 μm graphite flakes on the surface of a hafnia-silica DBR.

4.6 Conditioning Results

Long 1 second laser exposures caused a reduction in absorption for irradiances of 11 kWcm^{-2} and higher, see figure 4.9. Significant absorption occurred beginning at an obvious threshold near 20 kWcm^{-2}. This agrees well with the conditioning threshold that was estimated by comparing a laser spot to the area of particle removal, see chapter 3. Higher irradiances were found to cause greater sample conditioning with final absorption values after laser exposure being reduced by upwards of 90% of their original values.

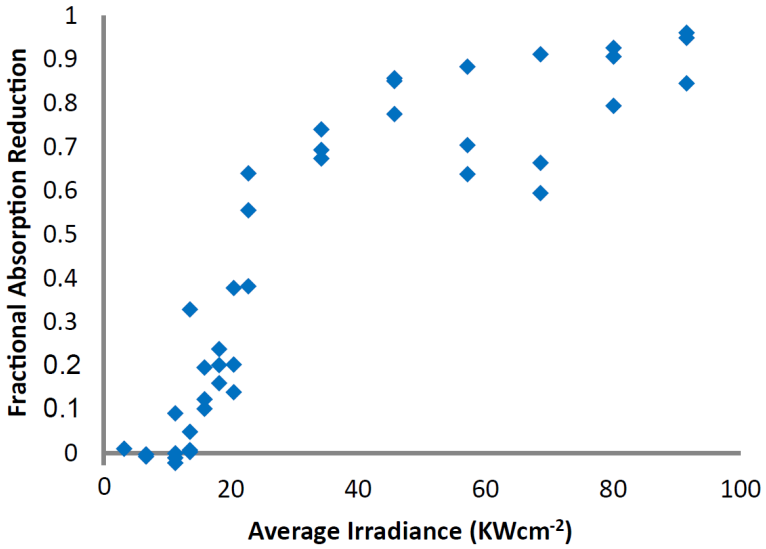

Figure 4.9: Absorption reduction vs. irradiance for 1 second laser exposure of hafnia-silica DBRs with 1 μm graphite flakes. Note the threshold irradiance near 20 kWcm^{-2} required for significant absorption change. The increase in absorption for irradiances below 15 kWcm^{-2} is due to the particles thermally bonding to the film

Tests conducted at 34 kWcm^{-2} for different exposure lengths revealed a minimum exposure time of 100 μs was required for any absorption change to occur, see figure 4.10. Once conditioning was underway, absorption changes for a given time were varied, though they trended upwards towards more thorough conditioning for longer exposures. The final absorption values at 300 ms and 1 second closely matched near 75% absorption reduction, indicating that the conditioning process was complete and the extra 700 ms of exposure in the 1 second tests did little to further the conditioning process.

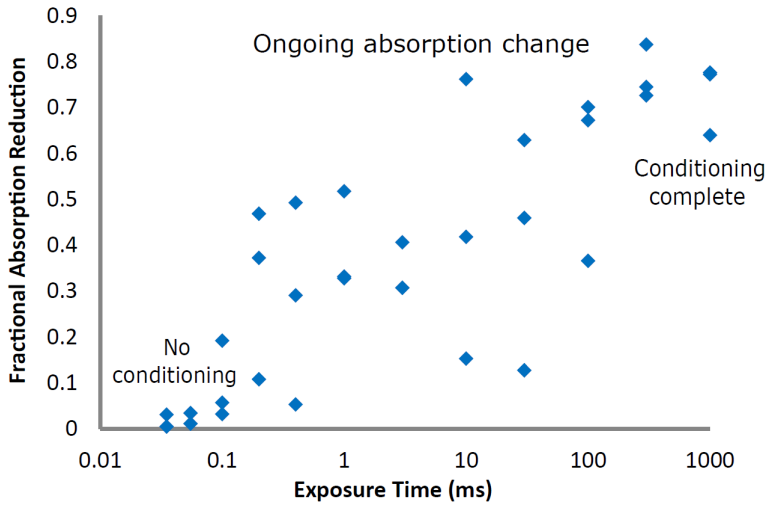

Figure 4.10: Particle absorption reduction vs. exposure time for 34 kWcm^{-2} irradiance. Note that the first absorption change occurs around 100 μs, and the final absorption values are reached by 300 ms.

Optical microscope images of the 34 kWcm^{-2} conditioned areas showed that many particles were fragmented, with some being completely removed, see figure 4.11. Small areas of translucent, reddish halos are seen to appear around some particles. Longer exposures more thoroughly removed particles within the beam spot and areas covered by the reddish residue became quite large, covering an area equal to or greater than that of the original particles. A sample was prepared to examine the residue using a scanning electron microscope (SEM). To aid in finding the conditioned area, the PCI pump laser was scanned across the surface at 10 W to create a line of conditioning that could be easily identified. Several nanometers of platinum where evaporated onto the surface to prevent static charging from the electron beam. SEM images confirmed that the reddish hue is a flat residue on the surface of the substrate, see figure 4.12. The residue is mechanically affixed to the surface, and could not be removed by drag wipe cleaning. Earlier composition studies of such residue had found it to be high in hydrocarbon species, see chapter 3. Images taken before 100 μs show no visible particle changes, and images taken at 300 ms and 1 second are virtually identical regarding the extent of conditioning. This agrees with the PCI data of figure 4.10, indicating the minimum exposures required to begin and finalize conditioning.

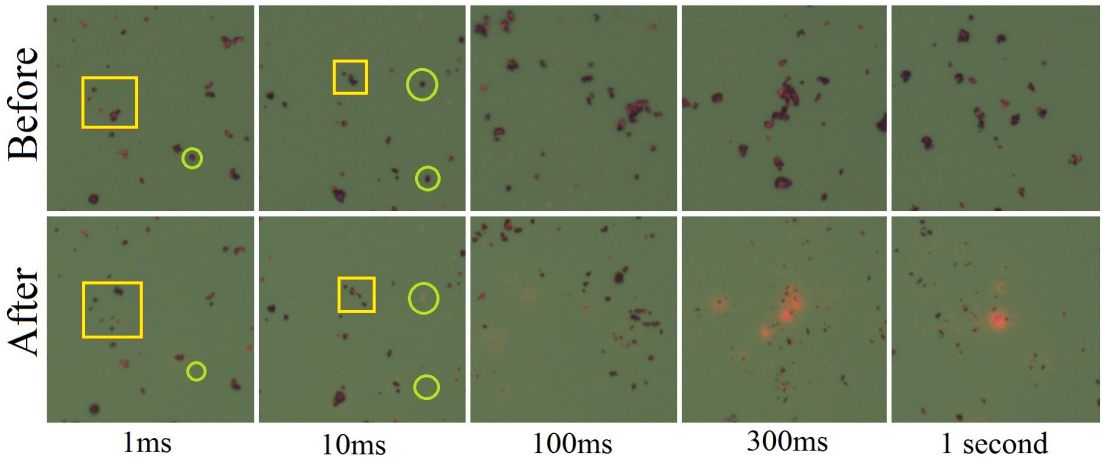

Figure 4.11: Particles before (top) and after (bottom) laser exposure at 34 kWcm^{-2}. Particles are seen to fragment (squares) and be removed (circles). Faint reddish halos are seen around some particles, indicating a local surface change. Longer exposures more thoroughly remove particles, and the presence of a conditioned residue becomes obvious by 300 ms.

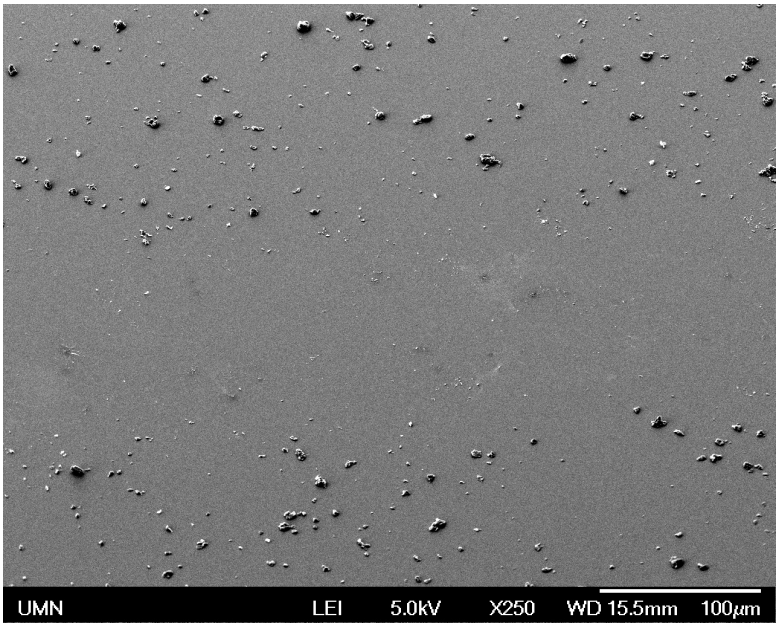

Figure 4.12: SEM image of particle removal. The flat residue left behind after scanning a laser across the surface is seen in the middle third of the image. The image was taken at 40° to highlight topography differences.

4.7 Discussion of Laser Conditioning

In order to better understand the laser conditioning process, it is useful to compare the measured conditioning timescales with those estimated from the physical properties of the particles. While calculating the energies entering the particles from laser irradiation and leaving from thermal radiation are relatively straightforward, estimating the thermal loss due to contact with the substrate is more uncertain. Thankfully the conditioning threshold for the graphite particles found using 1 second exposures provides a convenient means to estimate the thermal contact conductance (TCC) between the particles and the underlying substrate. At the threshold of conditioning, we assume the particle temperature is just high enough to reach the sublimation temperature of carbon, 4000 K [27]. Given steady state conditions, the power entering and leaving the particle at this temperature and irradiance are the same, allowing us to estimate the contact conductance with the substrate, see Equation 4.2.

$$TCC = \frac{A_{abs} * I_T - A_{emit} * \sigma * T_c^4}{T_c - T_s} \tag{4.2}$$

Where I_T the threshold irradiance, A_{abs} is the particle cross-sectional area absorbing incident light, A_{emit} is the particle area emitting thermal radiation, T_c the temperature required to condition (which we assume is the sublimation temperature of the carbon contaminant), T_s is the substrate temperature, and σ is the Stefan-Boltzmann constant. Note that the contaminants are assumed to be perfect blackbodies. Using a 10 μm hemisphere for the model particle, the TCC is estimated at 46 $\mathrm{kWm^{-2}K^{-1}}$. This value initially seems high in comparison to metal-metal contacts which have a TCC on the order of a few $\mathrm{kWm^{-2}K^{-1}}$ [28], however the TCC of graphene and highly ordered graphite can easily be tens of $\mathrm{MWm^{-2}K^{-1}}$ [29]. The loose bonding of the graphite with the surface of the optic and the agglomerated nature of the graphite flakes may explain the lower value calculated.

With this order-of-magnitude estimate, the temperature of a particle under irradiation can be roughly approximated. Simulating the heating of a model particle, the particle is estimated to reach its sublimation temperature within 240 μs for an irradiance of 34 $\mathrm{kWcm^{-2}}$, close to the 100-200 μs that was experimentally measured as the

minimum required exposure to cause absorption changes. In order to completely condition the surface, far more exposure time was required. This additional time is likely due to some particles thermally bonding to the substrate during the first part of exposure. Bonding of the particle and substrate increases the TCC. The substrate, now acting as a heat sink, increases the required exposure time to heat the particle and bonded film up to sufficient temperature to fully condition. Evidence of this bonding can be seen in the first several power steps of figure 4.7 and the lower irradiances of figure 4.9. At these low irradiances the measured absorption is seen to increase as the particles bond to the surface, transferring more heat into the substrate, and increasing the PCI signal.

4.8 Laser Conditioning Summary

Laser-conditioned contaminated optics display a minimum threshold intensity beyond which the surface absorption begins to decrease due to particle removal and fracturing. Photothermal common-path interferometry provides an effective means of characterizing the laser conditioning process as both a function of time and irradiance. For long duration exposures, a conditioning threshold irradiance of 20 $kWcm^{-2}$ was found to be required to cause significant absorption reduction of carbon microparticles. With high enough irradiances, conditioning reduced absorption by over 90%. Shorter exposures were also found to have a minimum time required to begin particle conditioning and also a minimum time required to reach full conditioning. Images of particles taken at different times show fragmentation, particle removal, and residue creation.

Simulation results using a thermal contact conductance found from the long duration conditioning threshold indicate that several hundred microseconds of exposure at 34 $kWcm^{-2}$ is enough to heat carbon particles to the point of sublimation. This agrees with some of the absorption reduction and particle change observed. The exposure time required to fully condition samples, however, is several hundred milliseconds at 34 $kWcm^{-2}$. The extra time required to fully condition is most likely due to the particles thermally bonding with the substrate. This is seen as a thin residue that covers much of the conditioned area. With the contamination and substrate in close thermal contact, more energy, and thus more exposure time ,is required to heat the thermal mass to the point of being fully conditioned.

4.9 Free Carrier Absorption in Microheater Films

In addition to measuring the absorption of optical coatings, our PCI system also proved useful for other experiments as well. One such experiment was a direct measurement of free carrier absorption at elevated temperatures. Free carrier absorption is an important physical process that affects laser breakdown of optics. Unfortunately there are few actual absorption values listed in the literature, especially at the elevated temperatures of interest for laser damage.

To heat an optical film to sufficient temperatures, microheaters with a Ti/Pt resistive trace were fabricated on silicon wafers with a 100 nm ALD alumina film, see figure 4.13(a). For microheaters that were etch released, the only absorption expected is from the bandgap large 7 eV bandgap alumina film. Microheaters that were not etch released have the heated silicon substrate with significantly more free carriers at a given temperature.

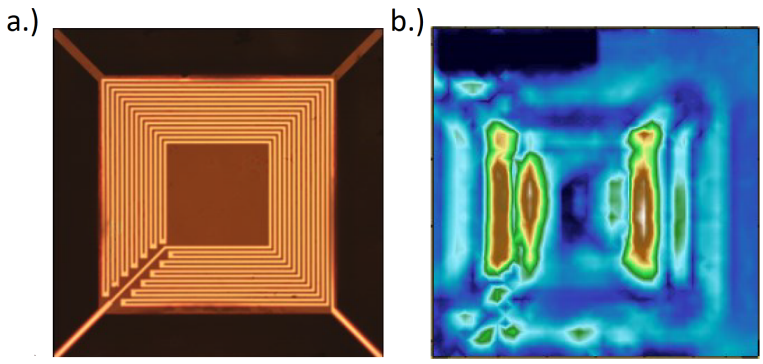

Figure 4.13: a.) Microheater fabricated on an ALD alumina film. b.) 2D PCI scan used to locate the center of the microheater

The small size of the central region of the microheater made aligning the sample in the PCI system challenging. 2D surface scans were used to precisely find the xy center of the microheater, see figure 4.13(b). This was followed by a longitudinal scan to find the maximum absorption either at the surface of the alumina or the underlying silicon depending on if the heater had been etch released.

Current was supplied to the microheaters while the absorption was measured using the PCI. Temperature at a given current had previously been determined by measuring

the microheaters' black body emission. When the absorption vs. temperature was plotted, the exponential increase in absorption due to the free carrier contribution is readily apparent, see figure 4.14. As expected free carriers in the silicon of the non-etch released microheaters dominated the absorption at high temperature. The etch released microheaters had no measurable absorption change as the temperatures reached in testing were too low to excite carriers in the alumina film.

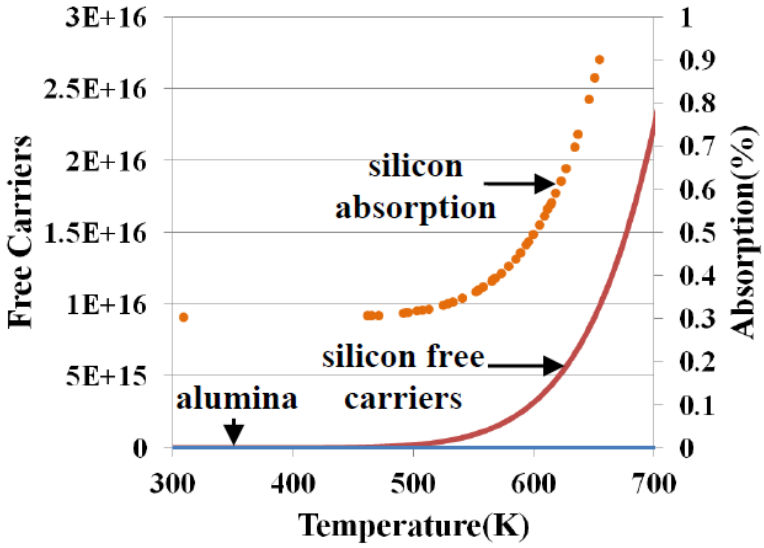

Figure 4.14: Measured absorption and carrier density for silicon. The alumina film with its larger bandgap did not meaningfully increase in absorption at the temperatures measured.

Chapter 5

Bandgap Dependence of CW Particle Induced Laser Damage

5.1 Motivation and Prior Research

The influence of material bandgap on short pulsed laser damage is well known, and widely reported in the literature. Such breakdown at high electric fields and irradiances is attributed to multiphoton absorption and impact ionization processes followed by free carrier absorption [17, 3], see chapter 2. Due to these effects, large bandgap materials perform favorably in resisting pulsed laser damage [4]. Continuous-Wave (CW) sources lack the photon fluxes of pulsed lasers, making both multiphoton absorption and impact ionization statistically improbable. CW laser damage is instead attributed to thermal effects leading to film stress, cracking, and delamination [19]. The bandgap of a material is normally not considered important in selecting optical coatings for use with CW lasers, instead priority is given to using the lowest absorption films to minimize possible thermal effects. Finding low absorption materials and deposition techniques has advanced coatings for CW systems, with five decades of research creating optics capable of operating at average powers of hundreds to thousands of kW/cm^2 in clean environments while maintaining consistent optical properties [17, 18].

Unfortunately for optical designers, the world is not a clean room. Contamination, whether from manufacturing, environmental, or human sources is all but inevitable. As

seen in chapter 3, contaminants can easily lower damage thresholds by orders of magnitude, meaning that the practical damage threshold is usually limited by cleanliness rather than intrinsic materials or film absorption [30, 9, 16]. Further complicating the issue is that the majority of laser damage experiments use carefully controlled laboratory conditions with lasers focused to small spots on clean, pristine materials. The overwhelming majority of optical failure occurs under radically different conditions. Understanding how surface contamination initiates damage and determining what can be done to mitigate its effects are crucial for designing optics that can survive in typical (dirty) conditions.

The first hints that thermal properties may not be the deciding factor for CW damage came when testing tantala-silica and hafnia-silica distributed Bragg reflectors (DBRs). Despite having lower absorption (1 ppm vs. 7 ppm) and higher thermal conductivity (3 $Wm^{-1}K^{-1}$ vs. 1.2 $Wm^{-1}K^{-1}$) the tantala-silica DBR's performed worse when contaminated with carbon particles, see chapter 3. The bandgap energy of hafnia films is significantly higher at 5.7 eV vs. 4.3 eV, leading us to suspect that it plays a role in determining particle induced laser damage.

5.2 Optics and Contaminants Tested

To see if other materials also followed the bandgap behavior, addition optical coatings were added to the testing. Titania-silica and niobia-silica high reflectivity DBRs were added to the tantala-silica and hafnia-silica, giving a bandgap range of 3 ev to 5.7 eV for the non-silica material. Half wave ($\lambda/2$) coatings were also added to the testing. These coatings were titania, tantala, hafnia, alumina, and silica, with bandgap energies ranging from 3 eV to 9 eV. All the coatings were deposited by ion beam sputtering (IBS) on 1 inch fused silica superpolished optical flats and designed for a center wavelength of 1064-1070 nm, corresponding to the emission wavelengths of Nd^{3+}:YAG solid-state and ytterbium-doped fiber lasers. Prior to contamination, optical absorption values of these samples were measured to be between 0.7 ppm and 35 ppm using photothermal common-path interferometry (PCI), see table 5.1.

Large absorbing particles are known to dramatically reduce damage thresholds [16, 15]. Carbon-based contamination, as is often encountered in routine handling or

Table 5.1: Material properties of the films tested. The absorption before contamination, thermal conductivity, melting point, and bandgap energy are listed. Of these parameters, only the bandgap matches the laser damage results of both $\lambda/2$, and DBR coatings. [31, 32, 33, 34, 35, 36, 37, 38]

Film Material	Absorption (ppm)	Thermal Conductivity ($Wm^{-1}K^{-1}$)	Melting Point (K)	Bandgap (eV)
Titania	3.5 ppm $\lambda/2$	3	2048	3
Niobia	2 ppm DBR	1.5	1793	3.85
Tantala	12 ppm $\lambda/2$, 0.7 ppm DBR	3	2191	4.3
Hafnia	35 ppm $\lambda/2$, 20 ppm DBR	1.2	3031	5.7
Alumina	30 ppm $\lambda/2$	1.1	2345	7
Silica	1.5 ppm $\lambda/2$	1.1	1996	9

environmental exposure, is particularly problematic, see chapter 3. For this reason, carbon microparticles were selected as the primary test contaminant. Stainless steel microparticles of diameter 35-40 μm were also used as a contaminant in some tests since metallic particles are a frequently encountered contaminant created during the assembly of optical systems [15, 39]. The optical surfaces were contaminated in the same fashion as before, using a suspension of microparticles in isopropyl alcohol. The absorption of the surface after contamination was measured using photo thermal common path interferometry (PCI), see figure 5.1. The spot size of the PCI pump laser was 56 μm. The much larger spot of the laser used in the damage testing, effectively averages out the small local absorption variations.

Laser damage testing was again conducted at Penn State's Electro-Optics Center using their 17 kW CW Ytterbium Doped fiber laser at 1070 nm to illuminate samples. The high power of the laser permitted testing of several $MWcm^{-2}$ irradiances with spot sizes on the order of a millimeter. Weaker lasers must sacrifice spot size for irradiance, and can often only illuminate diameters of tens of μm^2. The larger spot sizes used in our testing are advantageous as they represent a better average of typical regions of an optic, with many defects or contaminants being illuminated. The Primes power meter was used as a water cooled beam dump to catch all the reflected or transmitted light off the samples. This had the advantage over the previously used graphite beam dumps of not out-gassing carbon into the air. Single shots were conducted at each location, stepping up the laser power until failure occurred. A thermal camera monitoring the

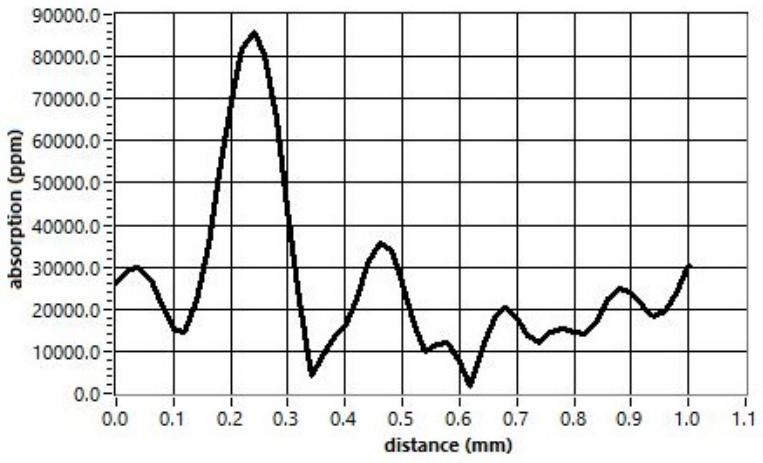

Figure 5.1: PCI scan across the surface of a carbon contaminated sample.

sample during testing provided information about the approximate surface temperature of the optic and could qualitatively tell how close a sample was to failure. Once a failure had occurred, irradiances above and below it were tested with the goal of finding an irradiance that caused damage for 50% of exposures. Variations in the contamination density cause differences in the damage threshold from location to location. For this reason reporting the minimum damaging irradiance and the maximum survived irradiance better captures the true spread of the data.

A fresh sample location was used for each shot to prevent any prior exposure from conditioning the sample and increasing damage thresholds, see chapter 4. For some catastrophic damage, debris ejected from the damage crater visibly contaminated the surface of the sample. These samples were retired from further testing to prevent the additional debris from influencing the results. Three to four samples of each material and contamination type were tested and the results combined to give the minimum damaging irradiance and the maximum survived irradiance. Samples were exposed to high power laser illumination for 10-30 seconds; however, failures always occurred essentially instantaneously to human perception.

5.3 LIDTs vs. Bandgap: Results

During testing, the carbon contaminated DBR coatings failed at irradiances as low as 17 kWcm^{-2} for titania-silica while hafnia-silica started to fail at 2.25 MWcm^{-2}. When damage occurred to a DBR, the optic failed catastrophically with the laser boring several millimeters into the fused silica substrate before the laser could be shut off manually. Comparing the damage thresholds to the bandgap energy of each film, a clear trend of increasing damage thresholds with larger bandgap energy is readily apparent, see figure 5.2. Stainless steel contaminated DBRs also displayed a similar bandgap dependence.

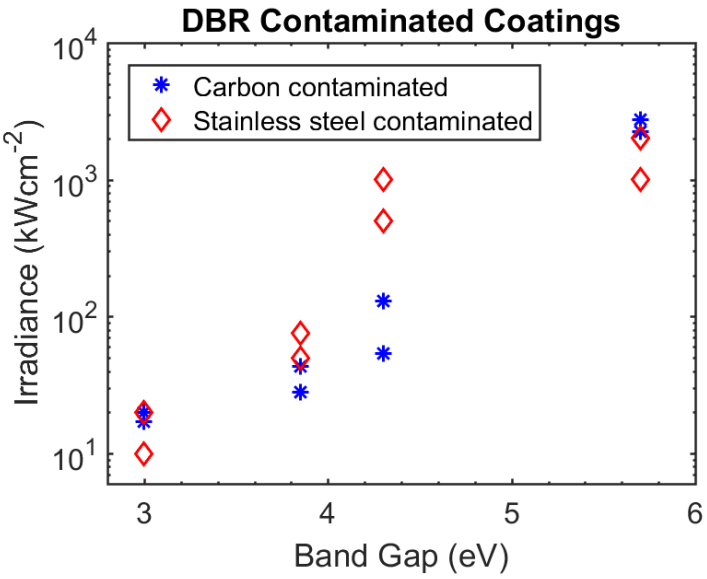

Figure 5.2: Laser-induced damage thresholds for microparticle carbon and stainless steel contaminated DBR coatings. Lowest damaging and highest survived irradiances are plotted for each material. Notice the clear trend of increasing damage thresholds with bandgap energy.

The carbon contaminated $\lambda/2$ coatings failed at irradiances as low as 105 kWcm^{-2} for titania films while silica coatings all survived the maximum tested irradiance of 17.8 MWcm^{-2}. All materials closely followed the bandgap trend over all the test irradiances, see figure 5.3. When damaged, the top film layer cracked, delaminated, or was removed completely from the underlying substrate though in most cases damage was self limiting and no deeper substrate damage occurred, see figure 5.4. The limited extent of the

damage in the $\lambda/2$ coatings made determining the damage threshold more difficult as many films showed small modifications to the surface even if damage was not initiated. This was especially true for the alumina coating that tended to fracture rather than delaminate.

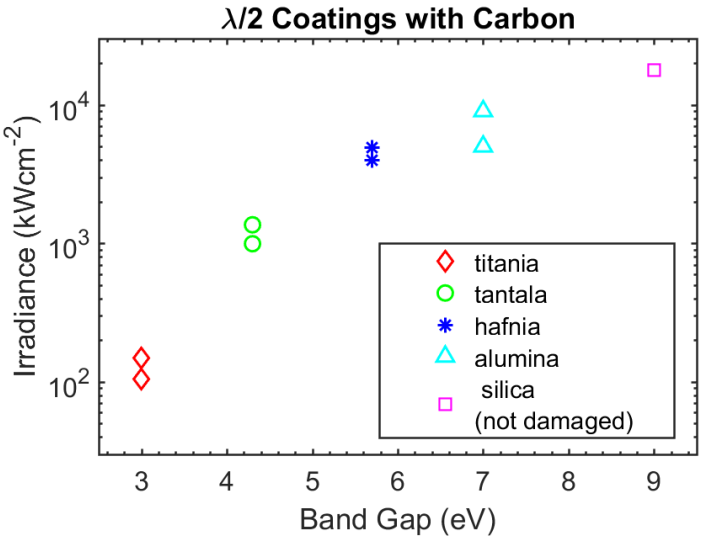

Figure 5.3: Laser-induced damage thresholds for microparticle carbon-contaminated $\lambda/2$ coatings. Lowest damaging and highest survived irradiances are plotted for each material. Silica $\lambda/2$ coatings (9 eV) were not damaged in testing.

It is interesting to note that the DBR coatings fail at much lower irradiances than the $\lambda/2$ films. There are several factors that could contribute to the DBRs' early failures. The many interfaces between the DBR layers create thermal resistance, limiting the heat diffusion downwards. This confines the heat generated by surface contamination, increasing the film temperature and causing damage at lower irradiances. Thermal stress between the layers could also cause fracture and delamination.

5.4 UV Plank Emission: Free Carrier Generation

With the bandgap behavior known, free carrier generation and absorption were hypothesized as the most likely processes ultimately responsible for early failure; however,

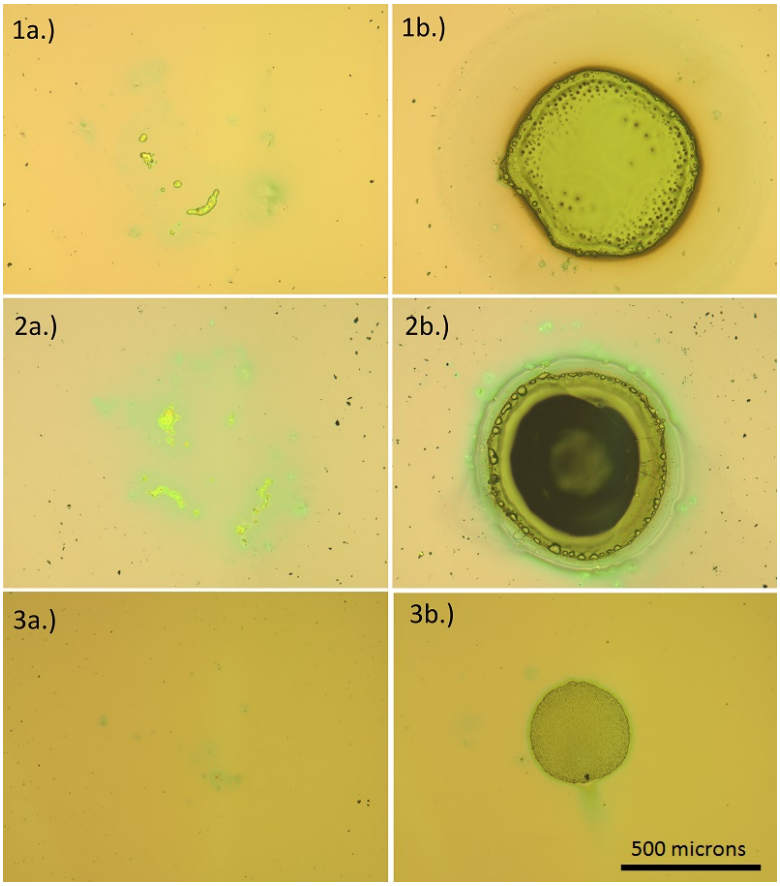

Figure 5.4: Carbon-contaminated $\lambda/2$ coatings after testing. 1a) titania at 128 kWcm^{-2} , 1b) titania at 155 kWcm^{-2} , 2a) tantala at 1 MWcm^{-2} , 2b) tantala at 1.5 MWcm^{-2}, 3a) hafnia at 3.6 MWcm^{-2} , 3b) hafnia at 8.3 MWcm^{-2}

the mechanism generating the free carriers was unknown. One of the potential free-carrier generation mechanisms was photoexcitation from the UV Planck emission of evaporating contaminant particles. Planck UV light, emitted from superheated surface contamination, could theoretically photo-excite carriers into the conduction band if the photon energy exceeds the bandgap of a material. This represents a possible source of free carriers that could initiate breakdown. This experiment was first done in Minnesota using the IPG Photonics 10 W PCI pump laser and a Photon Systems 224 nm 40 mW HeAg laser (HeAg 30-224SL). A calcium fluoride aspheric lens was used to focus the UV laser into as tight a spot as possible to generate the highest concentration of free

carriers. This spot was measured at less than 5 μm using a knife edge on a stage. No damage occurred to any pristine coatings during this experiment, but the difficulty of aligning two invisible lasers with micron sized beam diameters and short focal lengths made us suspect that the samples were not being exposed to the maximum irradiances.

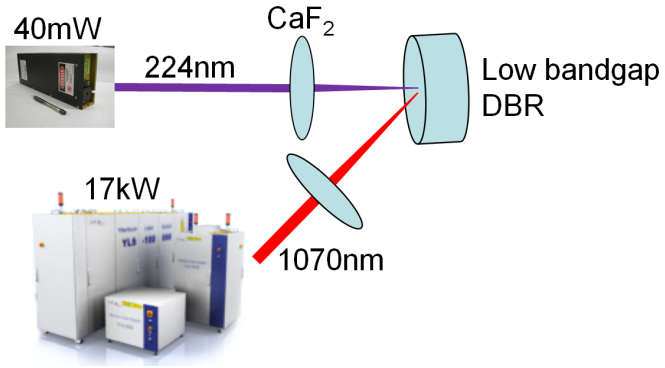

Figure 5.5: Experiment to test if UV photons could seed free carriers in a low bandgap material and initiate laser damage of a pristine sample.

To aid in aligning the beams, the experiment was conducted again at Penn State's EOC using their 17 kW 1070 nm laser, see figure 5.5. Titania-silica, niobia-silica, and tantala-silica DBR coatings were used for testing since the 224 nm laser has a photon energy that is significantly higher than their bandgap energies. The spot size of the 17 kW 1070 nm laser was varied between 0.5 and 1 mm, overlapping the UV-illuminated region with near-infrared laser power up to 13 MWcm^{-2}. The large spot size of the 1070 nm laser in comparison to the UV laser meant that the precise alignment of the two was not critical, though this was carefully done, and several tests were performed by rastering the surface to ensure that perfect overlap occurred. Because of the tight focus, and thus short depth of focus of the UV laser, tests were performed by moving the sample through the focus while simultaneously illuminating with both lasers to ensure that exposure occurred at the highest irradiances.

No damage from UV/IR illumination occurred despite illuminating samples with over 50 kWcm^{-2} of UV and 13 MWcm^{-2} of near-infrared, see table 5.2. Initially some random damage events happened during setup, though these were traced to airborne contamination left over from an unrelated experiment. After all the lab surfaces were wiped down with isopropyl alcohol and the room air filtered, no more damage events

occurred in the clean conditions. The UV irradiance produced by the HeAg laser is orders of magnitude greater than what could be generated from Plank emission of a superheated surface particle. The fact that this level of UV irradiance did not cause any failures despite exposing samples to 13 $MWcm^{-2}$ of near-infrared power, three orders of magnitude greater than the damage threshold with carbon contamination, effectively rules out UV photo-excitation as the damage mechanism for the contaminated optics.

Table 5.2: Number of tests of IR+UV illumination for each HR coating type. No damage from the combination of IR and UV exposure occurred even at the highest test irradiances. With carbon contamination titania-silica HR materials began failing at 17 $kWcm^{-2}$, niobia-silica at 28 $kWcm^{-2}$, and tantala-silica at 53 $kWcm^{-2}$.

DBR Type	500 $kWcm^{-2}$	1 $MWcm^{-2}$	2 $MWcm^{-2}$	3 $MWcm^{-2}$	3.4 $MWcm^{-2}$	5 $MWcm^{-2}$	11 $MWcm^{-2}$
titania-silica					3 tests		
niobia-silica	1 test	2 tests	2 tests	1 test	4 tests	1 test	16 tests
tantala-silica		1 test			3 tests	1 test	1 test

5.5 Capping Layers

With UV photogeneration effectively ruled out as a source of free carriers, thermal generation from direct contact with superheated surface contaminants was considered the most likely mechanism for seeding free carriers. One means of potentially increasing damage thresholds is to cap a low bandgap DBR with a thin material that is extremely robust in resisting contamination-induced breakdown, effectively insulating the DBR from the hot surface contamination. Silica, with a large bandgap and no failures in the $\lambda/2$ testing, was chosen as the cap layer. Cap layers with thicknesses equal to 3 to 15 half-waves (1.1-5.5 μm) were deposited over tantala-silica DBRs, see figure 5.6. They were contaminated with carbon and tested in the same fashion as the normal DBRs. To test very thick protective coatings, carbon was applied to the back surface of the silica substrate and the sample was illuminated from the backside, effectively using the substrate's thickness as a capping layer, see figure 5.6.

The samples with silica capping layers showed little to no improvement in damage thresholds over normal uncapped DBRs, see figure 5.7. This originally seemed at odds with any model involving direct thermal conduction from particle to substrate; however,

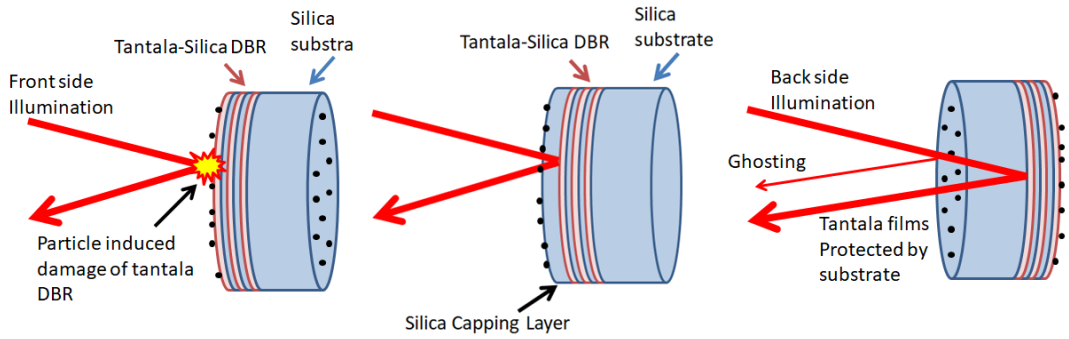

Figure 5.6: (Left) normal laser damage testing of a high reflectivity DBR. (Center) Protective capping layers to insulate surface particles from the low bandgap DBR. (Right) backside illumination using the thickness of the silica substrate as a very thick capping layer.

the thermal model of laser damage developed in the next chapter shows that the capping layer thickness was too thin to effectively insulate the low bandgap materials from the superheated surface contamination. Results of experiments where the substrates were contaminated on the backside and illuminated from the backside showed no failures up to the highest powers attainable. Here the capping layer thickness was effectively that of the entire substrate.

In the next chapter a model is developed for the thermal generation of free carriers by heated surface contaminants. It is demonstrated that this model fits the experimental results of the half-wave coatings, predicting what irradiances thermal runaway occurs for differing material bandgap energies.

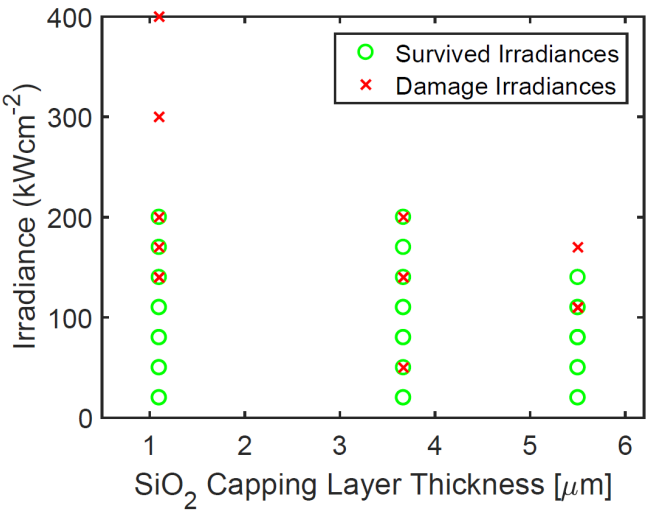

Figure 5.7: Laser damage tests of carbon contaminated tantala-silica DBRs with protective silica capping layers. There is no appreciable increase in the damage threshold for the thicker capping layers.

Chapter 6

Thermally Generated Free Carrier Breakdown Model

6.1 Heat Transfer into the Optical Coatings

Since free-carrier generation via heated surface contamination was consistent with our initial data (once the effects of capping layers and UV illumination were understood), we constructed a physical model to determine if it could predict the quantitative breakdown values that were experimentally observed. In this model, laser radiation is absorbed by a contaminant particle on the surface of an optical coating. The absorbed laser energy causes the particle temperature to rise to sublimation, and the particle begins to lose mass to evaporation. During this period, heat from optical absorption and the particle-film interface thermally generates free carriers in the film. If a sufficient concentration of carriers is generated, the subsequent free-carrier absorption creates a runaway thermal breakdown. However if the particle fully evaporates before sufficient free carriers are generated, heat ceases to be transferred into the coating and the optic will survive.

The optical absorption of the sample and the thermal contact conductance (TCC) between the particle and film are the key parameters that determine the heat transfer into the coating. The absorption of carbon-contaminated samples measured by photo thermal common-path interferometry (PCI) varied by location, with values of several tens of thousands being typical. The small size of the PCI's pump laser relative to the 0.4-1 mm laser spots used in testing ensures that the average absorption seen during

damage testing is far more consistent than the PCI measurement. In the model an average value of 20,000 ppm was used. TCC values were previous calculated at 46 $kWm^{-2}K^{-1}$ during laser conditioning experiments of 1 μm graphite flakes, see chapter 4. To gain an understanding of the meaning of this value, typical metal-metal mechanical contacts generally have a TCC on the order of a few $kWm^{-2}K^{-1}$ [28]. This low value indicates both the roughness and the weak incidental bonding of surfaces temporarily in mechanical contact. At the other extreme, the TCC of graphene and highly ordered graphite can easily be tens of $MWm^{-2}K^{-1}$ [29]. Due to the loose, disordered nature of the graphite flakes in our study, a value much lower than highly ordered graphite but somewhat larger than metal-metal contacts makes physical sense. The 7 μm carbon particles used in laser damage testing are relatively close in size and shape to the 1 μm graphite flakes for which the TCC estimate was calculated and for the model a TCC of 48 $kW^{-2}K^{-1}$ was found to best fit the experimental data.

Heat losses from radiation, air convection, and air conduction had to also be considered. Radiation losses emitted upwards from the particle and film surface were calculated by the Stefan-Boltzmann law and were included in the simulation, though their effect was minor. Coefficients for free air convection are typically less than 10 $Wm^{-2}K^{-1}$ [40], three orders of magnitude smaller than the estimated contact conductance between the particle and film and can safely be discounted. Air conduction with a thermal conductivity of 0.026 $Wm^{-1}K^{-1}$ and typical boundary layers of millimeters [41] is also three orders of magnitude smaller than the contact conductance, and was also discounted.

To calculate the heat flux from the particle into the film via contact conductance, the temperature of the particle must be known in addition to that of the film. During the first moments of exposure, the particle takes a finite amount of time to reach its sublimation temperature. Due to the energy required to vaporize a particle being roughly 10x the energy needed to reach its sublimation temperature, this short time span was disregarded. The evaporating particle is assumed to stabilize at its sublimation temperature [42], as previous studies with evaporating contaminants have shown the temperature gradient across such a particle to be minimal [43]. With the particle at its sublimation temperature, the evaporation rate of the particle is calculated from the incident laser power and carbon's heat of vaporization.

6.2 Heat Equation with Free Carrier Absorption

With the heat source terms known, the heat diffusion equation was used to solve for the temperature within the optical film during exposure. The particle-film interface is defined as a Neumann boundary condition with the heat flux crossing it determined by the optical absorption of the incident laser and the particle-film temperature difference with the estimated TCC. Heat entering through the boundary then diffuses downwards into the deeper layers of the film. Free carrier absorption is included as a bandgap and temperature dependent source term that adds heat within the film when sufficient carriers are generated, see equation 6.1.

$$\frac{\partial T}{\partial t} = D\nabla^2 T + \frac{\alpha_{FC} * I_{laser}}{\rho C} \tag{6.1}$$

D is the thermal diffusivity, α_{FC} is the free carrier absorption coefficient as a function of temperature and bandgap, I_{laser} is the irradiance of the incident laser, ρ is the density, and C is the heat capacity. To calculate the free carrier absorption, the Drude-Lorentz model of an electron plasma is used to estimate the imaginary part of the dielectric constant, which is then related to the absorption coefficient see equation 6.2 [44].

$$\alpha_{FC} = \frac{Ne^2}{m^* \epsilon_0 nc\tau} \frac{1}{\omega^2} \tag{6.2}$$

N is the density of free carriers, τ the phonon lifetime, and ω is the angular frequency of the incident light. The effective mass, m^*, is taken to be the free space electron mass as the amorphous films lack the band curvature in k-space. The density of carriers N is simply calculated from density of states and the Maxwell Boltzmann distribution of energies, see equation 6.3 [45].

$$N = \sqrt{N_c N_v} \exp \frac{-E_G}{2k_B T} \tag{6.3}$$

N_c and N_v are the effective density of states of the oxide band edges, and E_G is the material bandgap.

6.3 Material Properties in Model

One difficulty encountered was obtaining data for the effective densities of states and phonon lifetimes in amorphous insulators. Such information is very sparse. Experiments with X-ray emission and quantum yield spectra find that amorphous SiO_2 and α-quartz share very similar electronic structure [46] [47]. Using numerical calculations based on the Hartree-Fock and density functional theory, a density of states of $3.5\text{x}10^{22}$ cm^{-3} was found for α-quartz [48]. Due to a lack of information about the other coating materials, the density of states for SiO_2 was used throughout the model.

For amorphous materials it is general practice to assume thermal transport is a series of random walks due to the disordered nature of the material. This results in an average phonon mean free path equal to the atomic spacing [49]. Dividing this by the speed of sound in the material gives the average phonon lifetime τ. Phonons also contribute to a reduction of bandgap energy. Disorder or variations of bond lengths within a material, give rise to extended tail states at the band edges, narrowing the bandgap, see figure 6.1(a) [50, 51]. At high temperatures the contribution to disorder from phonons exceeds that of the frozen-in disorder of the amorphous material, see figure 6.1(b) [50]. This bandgap reduction was incorporated into the free carrier calculation by using experimental data from fused silica and scaling with respect to the relative bandgap energy. Without this bandgap reduction, the predicted temperatures required to cause thermal runaway were roughly 1000 K too high to be realistic.

6.4 Solving the Heat Equation Numerically

Initially only the TCC between the particle and substrate was considered for the heat flux into the film. To solve equation 6.1, Mathematica was first used assuming a 1-D geometry to simplify solving the equation. Though Mathematica could easily solve the heat diffusion, it could not solve the nonlinear free carrier absorption term. For this reason the model was moved to MATLAB. Though significantly slower, the initial-boundary value solver for parabolic-elliptic PDEs (PDEPE) was able to handle the free carrier term as a heat source and solve equation 6.1, though it was limited to 1-D solutions. To better capture the heat transfer both downwards and outwards, a spherical approximation can be used, see figure 6.2. Since we have determined the particle mass

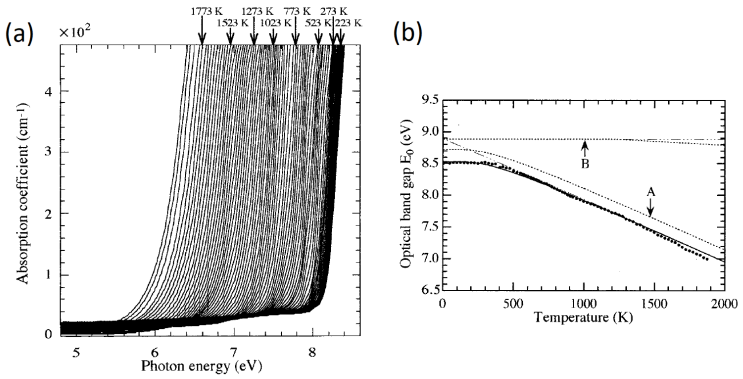

Figure 6.1: (a) VUV absorption spectrum of 120 μm thick fused silica at high temperatures showing optical bandgap reduction. (b) Fused silica's optical bandgap. Dotted lines A and B are contributions from phonons and structural disorder respectively. Notice for high temperatures thermal vibrations dominate the bandgap reduction and the structural disorder from the material being amorphous is minor in comparison. Figures from [50]

loss above, the time it takes to completely remove the particle from the substrate can be calculated. When the entire volume of the particle has been vaporized, the heat flux from the particle into the underlying material vanishes, and the surface will begin to cool. If, however, sufficient surface temperatures are reached before the particle has fully evaporated, the free carrier absorption will begin to dominate the heat transfer, and the near-surface material will thermally run-away. Survival could be seen when the particle fully evaporated, and damage could be seen as an exponential increase in the surface temperature when free carriers began to dominate, see figure 6.3.

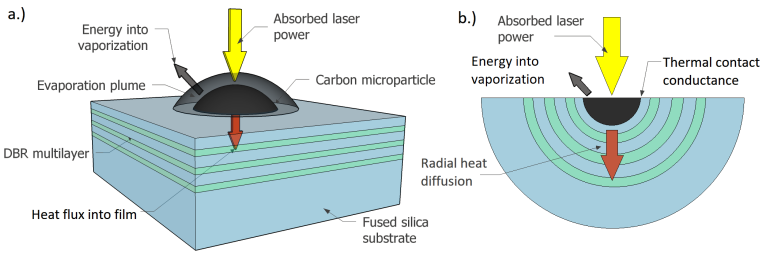

Figure 6.2: (a) Power entering an optical coating. The energy lost to evaporation is balanced by the energy transfered into the film. (b) 1-D spherical symmetry used to approximate the solution.

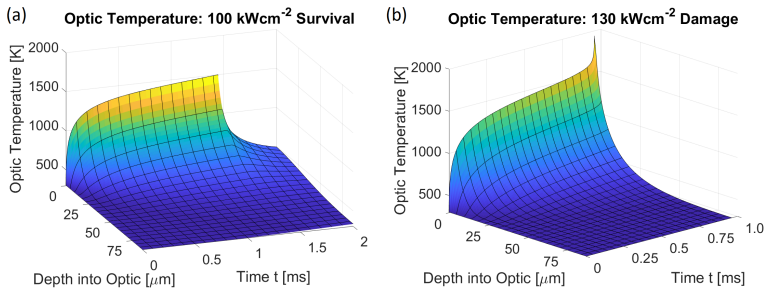

Figure 6.3: Simulated optic temperature for an optic (a) surviving 100 kWcm^{-2} and (b) failing at 130 kWcm^{-2}

Initial results with the 1-D spherical model were encouraging, however insufficient heat was being transfered into the film at higher irradiances to match the experimental damage thresholds. To match the data, the TCC used in the model had to increase with irradiance, see table 6.1. This made intuitive sense as the surface temperatures were higher and the top film layers and particle could be fusing together, increasing heat transfer.

Table 6.1: Simulation results of the four carbon contaminated DBRs. Notice the contact conductance that fits the experimental results increases at the higher irradiances and surface temperatures most likely as the particle begins to transform into a thin film and tightly bond with the underlying optic.

DBR Type	Irradiance (kWcm^{-2})	Calculated TCC (kWm^{-2}K^{-1})	Maximum Surface Temperature (K)	Evap Time (ms)
TiO_2-SiO_2	17-20	24-25	1127	20
Nb_2O_5-SiO_2	28-43	37-38	1380	5.0
Ta_2O_5-SiO_2	53-129	47-51	1566	1.0
HfO_2-SiO_2	2250-2740	165-177	2086	0.041

Forcing the model to match the data by using the TCC values though enlightening was less than ideal. Using the damage thresholds for the halfwave coatings, it was realized that by incorporating the absorption measurements from the PCI into the model, the predicted failures matched the experimental results. To more accurately capture both the heat flow outwards and down into the film, MATLAB's partial differential equation toolbox was used and the geometry of a particle on the surface could easily

be defined by using boundary conditions to represent the surface, see figure 6.4. Temperatures profiles throughout the materal could be simulated and damage was easily determined in the same fashion as an exponential increase in surface temperature see figure 6.5.

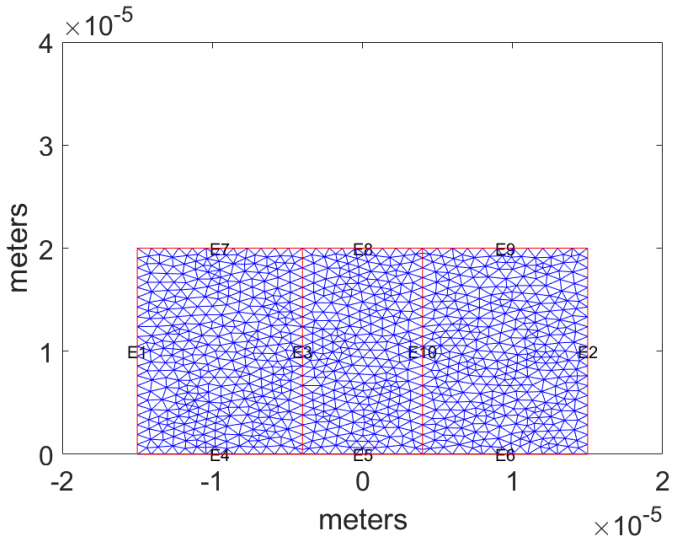

Figure 6.4: Meshgrid and edge boundary conditions used to simulate a particle resting on an optic's surface. Edge 8 incorporates the TCC and absorption as a flux term transferring heat into the film, while edges 7 and 9 lose heat to radiation.

Using the absorption value of 20,000 from the prior PCI measurements and the estimated TCC of 48 $\mathrm{kWm^{-2}K^{-1}}$ a close match to the experimental data was achieved, see figure 6.6.

6.5 Discussion

The thermal diffusion model explains the observed ineffectiveness of the silica capping layers in preventing laser damage. At the irradiances that caused damage to the capped tantala-silica DBRs, the carbon contamination takes roughly 1 ms to fully evaporate. This is sufficient time for heat to conduct the several microns through the cap layer and into the lower bandgap tantala, where it can generate free carriers and cause damage. For a capping layer to be effective, it must be substantially longer than the length heat

will diffuse during the evaporation time of particle contaminant, which for the example of tantala-silica DBRs would have been about 10 μm, twice that of the thickest capping layer tested. Backside illuminated samples have millimeters of silica that heat must diffuse through in order to reach the lower bandgap materials. This effectively insulates them from the particle heating and prevents any thermal generation of free carriers.

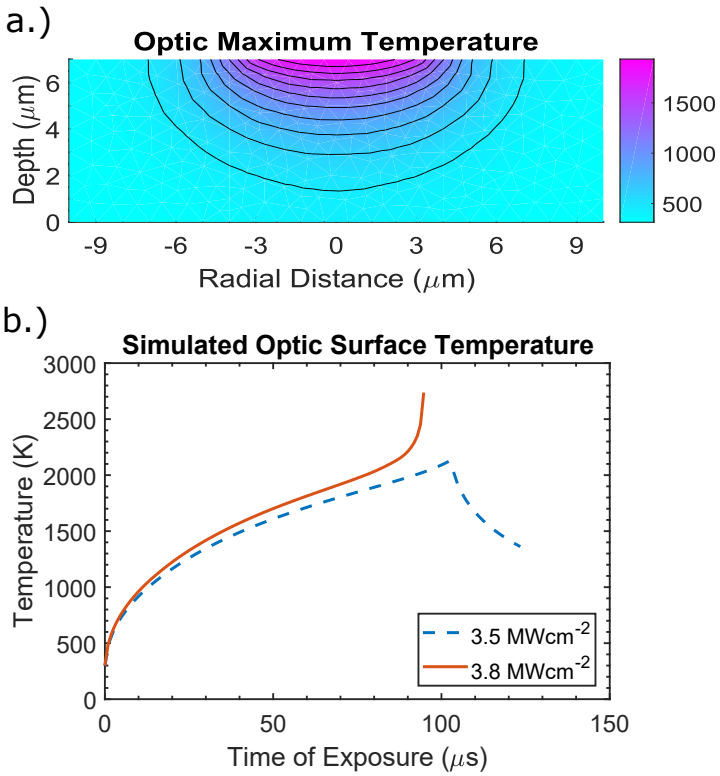

Figure 6.5: a.) Temperature of a tantala $\lambda/2$ coating at 3.5 MWcm^{-2} at the moment the carbon particle fully evaporates. b.) Simulated surface temperatures of a tantala $\lambda/2$ coating. The 3.5 MWcm^{-2} exposure fully evaporates the particle and the optic begins to cool while a 3.8 MWcm^{-2} exposure generates enough free carriers to cause thermal run-away.

The strong bandgap dependence of damage thresholds seen for all of the optical materials and contaminants is an interesting and unexpected result. Contamination has long been known to cause early failures optics under intense illumination

[30, 9, 15, 52, 53], however the seemingly random nature of failure has frustrated efforts understand the exact process or to even define a clear damage threshold for a material [17]. This perceived randomness has caused particle-induced breakdown to be treated statistically often without a physical basis and where probabilities of failure gradually increase with irradiance [17]. Differences in the composition of the contamination, the average size and shape of the contaminants, and wide variations in thin film properties due to different deposition techniques and conditions all further add to the observed spread of damage thresholds. Though some particle/defect-induced breakdown models have been developed, they typically analyze thermal shock and film stress caused by uneven heating [18] [16] [54]. In our study, while heat transfer into and within the material is certainly important, none of the standard thermal parameters of thermal conductivity, melting point, and intrinsic film absorption fit the observed damage thresholds, see table 5.1. Only differences in material bandgap are consistent with experimental observations. These observations show that low bandgap materials are a significant liability in high power optics if contamination is possible.

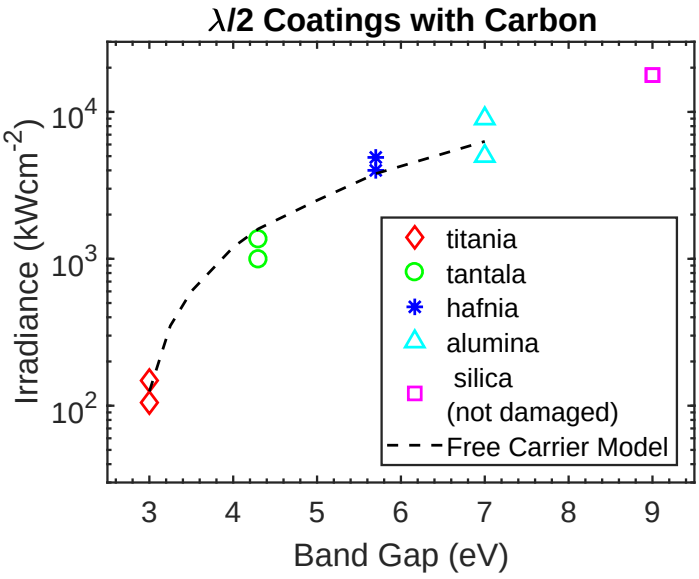

Figure 6.6: Laser-induced damage thresholds for microparticle carbon-contaminated $\lambda/2$ coatings. The dashed line represents thermally generated free carrier induced breakdown as predicted by our model.

In contrast to prior statistical treatments, our model is deterministic in describing

the laser damage process. For a given particle, optical material survival is determined by the bandgap of the material, the size of the contaminant that dictates the evaporation time, the optical absorption of the sample, and the TCC between particle and material. Statistics still play a role since higher contamination densities are more likely have particles or groups of clumped particles with sufficient mass and TCC to generate breakdown, but for each particle damage is simply a function of the above factors.

6.6 Conclusion

Contamination-induced breakdown is found to be a physically deterministic process that depends strongly on the bandgap of the materials underlying the contamination. This trend was observed for both $\lambda/2$ and DBR coatings and for both carbon and stainless steel contamination. Free carriers generated by interface thermal contact between the evaporating surface contaminants and the optical films/substrates are found to be the primary mechanism initiating failure. A physical model of heat transfer and free carrier absorption was developed that fits the experimental data with expected values for the absorption and thermal contact conductance. Engineers designing optics for high-power systems should choose high bandgap materials and optical coatings for the top several microns of the optical surface in order to avoid contamination-induced failure.

References

[1] B. C. Stuart, M. D. Feit, A. M. Rubenchik, B. W. Shore, and M. D. Perry. Laser-induced damage in dielectrics with nanosecond to subpicosecond pulses. 74(12):2248.

[2] Matthias Lenzner, Jrg Krger, S. Sartania, Z. Cheng, Ch Spielmann, G. Mourou, Wolfgang Kautek, and Ferenc Krausz. Femtosecond optical breakdown in dielectrics. 80(18):4076.

[3] M. Mero, J. Liu, W. Rudolph, D. Ristau, and K. Starke. Scaling laws of femtosecond laser pulse induced breakdown in oxide films. 71(11).

[4] Chris B. Schaffer, Andr Brodeur, and Eric Mazur. Laser-induced breakdown and damage in bulk transparent materials induced by tightly focused femtosecond laser pulses. 12(11):1784.

[5] J. Jasapara, A. V. V. Nampoothiri, W. Rudolph, D. Ristau, and K. Starke. Femtosecond laser pulse induced breakdown in dielectric thin films. 63(4).

[6] L. V. Keldysh. Ionization in the field of a strong electromagnetic wave. 20(5):1307–1314.

[7] Roger M. Wood. *Laser Damage in Optical Materials*. A. Hilger. Google-Books-ID: oytRAAAAMAAJ.

[8] Jh Campbell, F Rainer, M Kozlowski, Cr Wolfe, I Thomas, and F Milanovich. Damage resistant optics for a mega-joule solid-state laser. In He Bennett, Ll Chase, Ah Guenther, Be Newnam, and Mj Soileau, editors, *Laser-Induced Damage in Optical Materials: 1990*, pages 444–444–13. ASTM International.

[9] James R. Palmer. Continuous wave laser damage on optical components. 22(4):224435–224435.

[10] Frank M. Anthony. High heat load optics: an historical overview. 34(2):313–321.

[11] Yejia Xu, Amir Khabbazi, Travis Day, Andrew Brown, Luke A. Emmert, Joseph J. Talghader, Ella Field, Damon Kletecka, John Bellum, Dinesh Patel, Carmen S. Menoni, and Wolfgang Rudolph. Comparative STEREO-LID (spatio-TEmporally REsolved optical laser-induced damage) studies of critical defect distributions in IBS, ALD, and electron-beam coated dielectric films. volume 9632, page 963215. International Society for Optics and Photonics.

[12] Gary W. DeBell. Ion beam sputtered coatings for high fluence applications. page 599116.

[13] Nicholas Theodore Gabriel. High-power and high-aspect-ratio optical coatings by atomic layer deposition.

[14] Riikka L. Puurunen. Surface chemistry of atomic layer deposition: A case study for the trimethylaluminum/water process. 97(12):121301.

[15] Mary A. Norton, Christopher J. Stolz, Eugene E. Donohue, William G. Hollingsworth, Kalvin Listiyo, James A. Pryatel, and Richard P. Hackel. Impact of contaminates on the laser damage threshold of 1ω HR coatings. In *Laser-Induced Damage in Optical Materials: 2005*, volume 5991, page 59910O. International Society for Optics and Photonics.

[16] S. R. Qiu, M. A. Norton, R. N. Raman, A. M. Rubenchik, C. D. Boley, A. Rigatti, P. B. Mirkarimi, C. J. Stolz, and M. J. Matthews. Impact of laser-contaminant interaction on the performance of the protective capping layer of 1 w high-reflection mirror coatings. 54(29):8607.

[17] Alan F. Stewart, Lynn Bonsall, Jerry R. Bettis, James Copland, Keith P. Healey, Gerald B. Charlton, William Hughes, and Juan C. Echeverry. Laser damage in multispectral optical coatings for the ABL. In *Laser-Induced Damage in Optical Materials: 1998*, pages 162–171. International Society for Optics and Photonics.

[18] Rashmi S. Shah, Justin J. Rey, and Alan F. Stewart. Limits of performance: CW laser damage. In Gregory J. Exarhos, Arthur H. Guenther, Keith L. Lewis, Detlev Ristau, M. J. Soileau, and Christopher J. Stolz, editors, *Proc. SPIE 6403*, pages 640305–640305–14.

[19] Hui Gong, Cheng F. Li, and Zhong Y. Li. CW-laser-induced thermal and mechanical damage in optical materials. In *Laser-Induced Damage in Optical Materials: 1998*, pages 576–583. International Society for Optics and Photonics.

[20] Mark R. Kozlowski, Michael C. Staggs, Frank Rainer, and J. H. Stathis. Laser conditioning and electronic defects of HfO2 and SiO2 thin films. In *Laser-Induced Damage in Optical Materials: 1990*, pages 269–282. International Society for Optics and Photonics.

[21] Todd E. Lizotte and Terence R. O'Keeffe. Chemical-free cleaning using excimer lasers. In *Photonics West'96*, pages 279–287. International Society for Optics and Photonics.

[22] Dae-Jin Kim, Yong-Kee Kim, Je-Kil Ryu, and Hyun-Jung Kim. Dry cleaning technology of silicon wafer with a line beam for semiconductor fabrication by KrF excimer laser. 41(7):4563.

[23] Yongfeng Lu, Wen D. Song, Minghui Hong, ZhongMin Ren, and Yuan W. Zheng. Laser surface cleaning: basic understanding, engineering efforts, and technical barriers. In *First International Symposium on Laser Precision Microfabrication (LPM2000)*, pages 371–379. International Society for Optics and Photonics.

[24] Andrew C. Tam, Wing P. Leung, Werner Zapka, and Winfrid Ziemlich. Laser-cleaning techniques for removal of surface particulates. 71(7):3515.

[25] Herve Bercegol. What is laser conditioning: a review focused on dielectric multilayers. In *Laser-Induced Damage in Optical Materials: 1998*, pages 421–426. International Society for Optics and Photonics.

[26] A. Alexandrovski, Martin Fejer, A. Markosian, and Roger Route. Photothermal common-path interferometry (PCI): new developments. In W. Andrew Clarkson,

Norman Hodgson, and Ramesh K. Shori, editors, *Proc. SPIE 7193*, pages 71930D–71930D–13.

[27] J Abrahamson. Graphite sublimation temperatures, carbon arcs and crystallite erosion. 12(2):119–141.

[28] E.G Wolff and D.A Schneider. Prediction of thermal contact resistance between polished surfaces. 41(22):3469–3482.

[29] Z. Chen, W. Jang, W. Bao, C. N. Lau, and C. Dames. Thermal contact resistance between graphene and silicon dioxide. 95(16):161910.

[30] Floyd E. Hovis, Bart A. Shepherd, Christopher T. Radcliffe, Andrew L. Bailey, and William T. Boswell. Optical damage at the part per million level: the role of trace contamination in laser-induced optical damage. In *Laser-Induced Damage in Optical Materials: 1993*, volume 2114, pages 145–154. International Society for Optics and Photonics.

[31] H Demiryont, James Sites, and Kent Geib. Effects of oxygen content on the optical properties of tantalum oxide films deposited by ion-beam sputtering. 24(4):490–495.

[32] Matthew D Pickett and R Stanley Williams. Sub-100 fJ and sub-nanosecond thermally driven threshold switching in niobium oxide crosspoint nanodevices. 23(21):215202.

[33] Cheng-Chung Lee, Jin-Cherng Hsu, and Daw-Heng Wong. Low loss niobium oxides film deposited by ion beam sputter deposition. 32(3):327–337.

[34] S.-M. Lee, David G. Cahill, and Thomas H. Allen. Thermal conductivity of sputtered oxide films. 52(1):253.

[35] S Akhtar, D. Ristau, and J Ebert. Thermal conductivity of dielectric films and correlation to damage threshold at 1064nm. In *Laser Induced Damage in Optical Materials*, pages 345–351.

[36] A. Callegari, E. Cartier, M. Gribelyuk, H. F. Okorn-Schmidt, and T. Zabel. Physical and electrical characterization of hafnium oxide and hafnium silicate sputtered films. 90(12):6466.

[37] S. Capone. Physical characterization of hafnium oxide thin films and their application as gas sensing devices. 16(6):3564.

[38] I Stark, M Stordeur, and F Syrowatka. Thermal conductivity of thin amorphous alumina films. page 6.

[39] Stphanie Palmier, Sverine Garcia, and Jean-Luc Rullier. Method to characterize superficial particulate pollution and to evaluate its impact on optical components under a high power laser. 47(8):084203.

[40] Abdul-Jabbar N Khalifa. Natural convective heat transfer coefficient a review: I. isolated vertical and horizontal surfaces. 42(4):491–504.

[41] V. P. Carey and J. C. Mollendorf. Measured variation of thermal boundary-layer thickness with prandtl number for laminar natural convection from a vertical uniform-heat-flux surface. 21(4):481–488.

[42] V. I. Bukatyi, A. M. Sagalakov, A. A. Tel'nikhin, and A. M. Shaiduk. Combustion of carbon particles in a powerful optical field. 15(6):727–731.

[43] Tirtha Mitra, Andrew K. Brown, David M. Bernot, Sage Defrances, and Joseph J. Talghader. Laser acceleration of absorbing particles. 26(6):6639–6652.

[44] Anthony Mark Fox. *Optical Properties of Solids*. Oxford University Press.

[45] Robert F. Pierret. *Advanced Semiconductor Fundamentals*. Addison-Wesley Publishing Company. Google-Books-ID: ShlTAAAAMAAJ.

[46] S. S. Nekrashevich and V. A. Gritsenko. Electronic structure of silicon dioxide (a review). 56(2):207–222.

[47] V. A. Gritsenko, J. B. Xu, R. W. M. Kwok, Y. H. Ng, and I. H. Wilson. Short range order and the nature of defects and traps in amorphous silicon oxynitride governed by the mott rule. 81(5):1054–1057.

[48] Elena Gnani, Susanna Reggiani, and Massimo Rudan. Density of states and group velocity of electrons in ${\mathrm{SiO}}_{2}$ calculated from a full band structure. 66(19):195205.

[49] Charles Kittel. Interpretation of the thermal conductivity of glasses. 75(6):972–974.

[50] K. Saito and A. J. Ikushima. Absorption edge in silica glass. 62(13):8584–8587.

[51] S. R. Elliott. *Physics of Amorphous Materials*. John Wiley & Sons, Incorporated. Google-Books-ID: WJ5LPgAACAAJ.

[52] Anne Fornier, C. Cordillot, D. Bernardino, O. Lam, Andre Roussel, B. Pinot, Bernard Geenen, Herve Leplan, and W. Alexandre. Catastrophic failure of contaminated fused-silica optics at 355 nm. In *Solid State Lasers for Application to Inertial Confinement Fusion: Second Annual International Conference*, volume 3047, pages 987–1000. International Society for Optics and Photonics.

[53] Francois Y. Genin, K. Michlitsch, James Furr, Mark R. Kozlowski, and Peter A. Krulevitch. Laser-induced damage of fused silica at 355 and 1064 nm initiated at aluminum contamination particles on the surface. In *Laser-Induced Damage in Optical Materials: 1996*, volume 2966, pages 126–139. International Society for Optics and Photonics.

[54] Michael D. Feit, Alexander M. Rubenchik, Douglas R. Faux, Robert A. Riddle, Arthur B. Shapiro, David C. Eder, Bernie M. Penetrante, David Milam, Francois Y. Genin, and Mark R. Kozlowski. Modeling of laser damage initiated by surface contamination. In *Laser-Induced Damage in Optical Materials: 1996*, volume 2966, pages 417–425. International Society for Optics and Photonics.